Title: Variant-to-gene mapping identifies *ARHGEF12* as a primary open-angle glaucoma effector gene operating within retinal ganglion cells

Authors: Vrathasha Vrathasha[1,2,†], Matthew C. Pahl[3,4,†], James A. Pippin[3,4], Sergei Nikonov[2], Jie He[1,2], Mina Halimitabrizi[1,2], Laxmi Moksha[1,2], Rebecca Salowe[1], Amy-Ann Edziah[1], Yuki Bradford[5], Yan Zhu[1], Harini V. Gudiseva[2], Venkata R. M. Chavali[2], Bruna Lopes da Costa[2], Anne Marie Berry[2], Peter M. J. Quinn[2], Qi N. Cui[1,2], Eydie Miller-Ellis[1], Prithvi S. Sankar[1], Ahmara G. Ross[1,2], Victoria Addis[1], Shefali S. Verma[6], Andrew D. Wells[3,6,7,8], Struan F. A. Grant[3,4,9,10,11, †], Joan M. O'Brien[1,2,†,*]

†Authors contributed equally

* Corresponding author: Penn Medicine Center for Genetics of Complex Disease, 25 N 38th St, Philadelphia, PA 19104 (joan.obrien@pennmedicine.upenn.edu; phone: 215-900-4204)

Affiliations:

1. Center for Genetics of Complex Disease, Department of Ophthalmology, University of Pennsylvania, Philadelphia, PA 19104, USA
2. F.M. Kirby Center for Molecular Ophthalmology, University of Pennsylvania, Philadelphia, PA 19104, USA
3. Center for Spatial and Functional Genomics, The Children's Hospital of Philadelphia, Philadelphia, PA 19104, USA.

4. Division of Human Genetics, The Children's Hospital of Philadelphia, Philadelphia, PA 19104, USA
5. Department of Medicine, Perelman School of Medicine, University of Pennsylvania, Philadelphia, PA 19104, USA.
6. Department of Pathology and Laboratory Medicine, Perelman School of Medicine, University of Pennsylvania, Philadelphia, PA, USA
7. Department of Pathology, The Children’s Hospital of Philadelphia, Philadelphia, PA 19104, USA
8. Institute for Immunology & Immune Health, Perelman School of Medicine, University of Pennsylvania, Philadelphia, PA 19104, USA
9. Department of Pediatrics, Perelman School of Medicine, University of Pennsylvania, Philadelphia, PA 19104, USA.
10. Department of Genetics, Perelman School of Medicine, University of Pennsylvania, Philadelphia, PA 19104, USA.
11. Division of Diabetes and Endocrinology, The Children’s Hospital of Philadelphia, 3615 Civic Center Boulevard, Philadelphia, PA 19104, USA

Abstract: Primary open-angle glaucoma (POAG), a leading cause of irreversible blindness, has a strong genetic basis. The Primary Open-Angle African Ancestry Glaucoma Genetics study previously identified 46 risk loci. To pinpoint causal variants and their corresponding effector genes, we analyzed gene expression, chromatin accessibility, and conformation in two ocular cell-types: trabecular meshwork cells (hTMCs) and retinal ganglion cells derived from induced pluripotent stem cells (hiPSC-RGCs). We identified 24 candidate genes in hTMCs and 56 in hiPSC-RGCs. The *ARHGEF12* gene was selected for further validation because it was nominated by local and distal promoter interactions in both cell-types and has reproducible prior evidence of its association with POAG. While its role in hTMCs is established, its function in RGCs is unclear. hiPSC-RGCs generated from a POAG donor homozygous for the risk allele showed reduced *ARHGEF12* expression, altered morphology, and disrupted neuronal activity. This framework enables functional evaluation of additional POAG risk variants.

70 **Introduction:**

71 Over the past two decades, genome-wide association studies (GWAS) have revealed
72 thousands of single-nucleotide polymorphisms (SNPs) that are statistically associated
73 with complex phenotypes and disease risk.[1-3] The vast majority of these GWAS-
74 implicated signals are located in non-coding regions of the genome, presumably
75 influencing disease susceptibility by altering the expression of one or more target genes.[4-
76 6] However, the assumption that the nearest gene to the GWAS-implicated signal
77 represents the true effector gene has proven insufficient. Instead, effector genes can be
78 located tens or hundreds of kilobases distal to regulatory elements due to long-range
79 interactions at the 3D genome level.[4,6-12] As GWAS itself does not unambiguously reveal
80 which target genes and cell types are affected by the discovered signals, this complexity
81 hinders the interpretation of potential disease mechanisms.[8,13-15]

82 Historically, the study of 3D genome organization has been challenging due to a
83 lack of relevant methodologies. However, over the past decade, chromosome
84 conformation capture (3C)-based techniques, such as Hi-C and its derivatives, have
85 enabled mapping of putative contacts across a range of genomic distances.[16,17]
86 Structural genomics approaches have been successfully applied to several complex
87 genetic disorders, implicating novel risk genes. For type 2 diabetes, 3D genomic
88 approaches revealed that a causal variant for the strongest signal in the *TCF7L2* gene[18,19]
89 also functions as a regulatory region for *ACSL5*.[20] Similar approaches in osteoporosis[6],
90 obesity[21-23], carpal tunnel syndrome[8], type 2 diabetes[24], and rheumatoid arthritis[25] have
91 similarly implicated novel causal target genes that drove functional follow-up studies.

92 However, such 3D genomic efforts in the context of primary open-angle glaucoma
93 (POAG) remain limited, despite the disease being a leading cause of irreversible
94 blindness worldwide.[26-28] POAG has a strong heritable component, ranging from 13% to
95 81%.[29-32] Several monogenic mutations have been reported for POAG, but only account
96 for 5% of all cases.[33-36] Thus far, GWAS analyses have identified 329 risk loci associated
97 with POAG and its related endophenotypes.[37-53] However, the vast majority of these loci
98 are harbored in non-coding areas of the genome and therefore do not directly pinpoint
99 the underlying specific gene(s), cell types, or mechanisms.[39] Translating these results to
100 biological insights requires systematic identification of putative causal variants and the
101 corresponding candidate effector genes, together with functional verification in either
102 cellular or animal models.[24,54-56] Indeed, Wang *et al* reported that using scATAC-seq-
103 derived peaks in the human retina could assign a SNP (rs4821699), located in the intronic
104 region of *TRIOBP,* as a contributing causal variant to glaucoma by altering the gene's
105 expression in retinal ganglion cells (RGCs).[12]
106 The Primary Open-Angle African Ancestry Glaucoma Genetics (POAAGG) study
107 previously conducted a GWAS on POAG in African ancestry individuals, identifying 46
108 risk loci.[37] In this study, we employed 3D-genomic approaches to implicate causal
109 variants and their corresponding effector genes at these POAG loci. We generated 3D
110 genomics data using two glaucoma-related ocular cell lines: human trabecular meshwork
111 cells (hTMCs) and retinal ganglion cells derived from human induced pluripotent stem
112 cells (hiPSC-RGCs), as gene regulatory elements are known to be cell-type and tissue-
113 specific. Our analyses implicated 24 genes in hTMCs and 56 genes in hiPSC-RGCs. The
114 *ARHGEF12* gene was prioritized for functional follow-up, as multiple signals in both cell

115 types contacted its promoter, and it displayed contacts to a fine-mapped SNP from our
116 prior GWAS.[37] Though this gene has an established role in intraocular pressure (IOP)
117 regulation in hTMCs,[41] its function in RGCs remains poorly understood. We detected
118 significant differences in the *ARHGEF12* mRNA expression, ultrastructure of cellular
119 organelles, and spike firing rate in disease-variant hiPSC-RGCs derived from POAG and
120 control subjects.
121
122 **Results:**
123 **Chromatin contact maps of hiPSC-RGCs and hTMCs**
124 First, we sought to implicate candidate causal variant-effector gene pairs for the 46
125 POAG-associated loci identified by the POAAGG study.[37] We used ATAC-seq to identify
126 putative cis-regulatory elements (cREs) harboring proxy SNPs in both cell types and used
127 promoter-focused Capture C in hTMCs and Hi-C in hiPSC-RGCs to capture chromatin
128 contacts. Additionally, we generated RNA-seq data for both models to contextualize gene
129 expression in these cells (**Fig. 1a**). For these experiments, three biological replicates were
130 sequenced at standard or higher depth, with the exception of hiPSC-RGCs Hi-C, which
131 was performed in duplicate (**Fig. S1a**). While Hi-C is a genome-wide approach, Promoter-
132 focused Capture C enriches for contacts specifically at promoters, which can contribute
133 to differences in contacts detected. Libraries passed other QC metrics, such as the
134 expected fragment size distribution and proportion of long-range cis-reads in the
135 chromatin interaction data (**Fig. S1b,c**).
136 First, we focused on identifying open chromatin regions (OCRs) that may act as
137 regulatory elements to influence gene expression. We identified 132,634 OCRs in hTMCs

138 and 255,543 OCRs in hiPSC-RGCs that were reproducible in at least two replicates in
139 each cell type. A subset of OCRs was shared in both cell types, with 47.5% of the OCRs
140 found in hTMCs and 26.7% of the OCRs found in hiPSC-RGCs also detected in the
141 reciprocal cell type (**Fig. 1b**). As expected, most OCRs were in non-coding regions such
142 as introns and intergenic regions (**Fig. 1c**).

143 We then mapped these OCRs to effector genes using matched chromatin
144 conformation data. We considered both proximal OCRs overlapping promoter regions
145 themselves and OCRs overlapping distal promoter-interacting regions defined by Hi-C or
146 Promoter-focused Capture C, as well as distal OCRs (**Fig. 1d**). The significant distal
147 promoter interaction regions were considered using either Chicago[57] for promoter-
148 focused Capture C data, and the combination of Mustache[58] and FitHiC2[59] to call
149 interaction in the hiPSC-RGC Hi-C data.[6,24] We intersected the resulting loop calls with
150 ATAC-seq peaks to define a set of promoter-interacting region OCRs (PIR-OCRs), which
151 may function as long-distance cis-regulatory elements to influence gene expression. We
152 further considered the set of OCRs located locally to a promoter (-1500/+500bp of the
153 TSS) to be promoter OCRs.

154 A comparable number of promoter contacts were detected in both hiPSC-RGCs
155 and hTMCs, with Hi-C also detecting many non-promoter contacts (**Fig. 1e**). A subset of
156 these interactions involved one or more promoters (promoter-to-promoter interactions;
157 p2p). Comparing the distance between these interactions, we detected that non-promoter
158 to promoter interactions called by hiPSC-RGC Hi-C were longer than those called by
159 Capture C in hTMCs. However, the same difference was not observed for promoter-to-
160 promoter interactions across cell types (**Fig. 1f**). Overall, our approach identified 34,709

161 OCRs in interactions with 17,977 distinct genes in hTMCs and 39,496 OCRs contacting
162 19,174 genes in hiPSC-RGCs (**Fig. S1d,e**).
163
164 **Promoter-open chromatin interactions correlate with gene expression**
165 Next, we validated the association of promoter contacts across OCRs in the context of
166 gene regulation. We first identified the number of OCRs called per gene, which was a
167 mean of 5.0 in hTMCs and 6.2 in hiPSC-RGCs (**Fig. 2a**). Similarly, we examined the
168 mean number of genes connected per OCR, which was 2.6 in hTMCs and 2.5 in hiPSC-
169 RGCs (**Fig. 2b**). Given that multiple genes may be implicated at a GWAS locus, we next
170 sought to characterize the promoter-promoter and promoter-regulatory elements. We
171 found 9.2% of genes in hiPSC-RGCs and 12.1% of genes in hTMCs were in promoter–
172 promoter interactions with at least one other distinct gene. The number of connected
173 OCRs per gene was positively correlated with gene expression across both cell types
174 (**Fig. 2c**), suggesting that these interactions capture functional regulatory elements.
175 Next, we examined whether the number of OCRs contacting promoters correlated
176 with differences in genes between the two cell types. We identified differentially
177 expressed genes between hiPSC-RGCs and hTMCs. Given that we expected large
178 differences in expression between these two cellular models, we employed stringent
179 criteria, as our primary goal in this analysis was to identify cellular marker genes. We
180 observed 2,831 genes enriched in hTMCs and 12,316 genes enriched in hiPSC-RGCs
181 (**Fig. S2a; Table S1**), which may reflect greater cellular diversity in generated hiPSC-
182 RGCs when compared to directly harvested hTMCs. Reassuringly, known TMC and
183 retinal neuron genes were detected, as the gene with the highest enrichment in hTMCs

184 was *Fibronectin 1*, which is related to flow through the TMCs (*FN1*)[60], while in hiPSC-
185 RGCs it was *Cerebellar Degeneration Related 1* (*CDR1*), which is involved in retinal
186 neuron survival.[61] Likewise, pathway enrichment analysis revealed enrichment of
187 cytoskeletal, adhesion, and stress response pathways in hTMCs, which are all consistent
188 with the clinical reduction of aqueous humor flow through hTMCs in POAG. Rhodopsin
189 signaling, which plays an essential role in converting light into electrical pulses, displayed
190 the strongest enrichment in hiPSC-RGCs (FDR = 0.08) (**Fig. S2b**). When we correlated
191 the difference in the number of OCR contacts with gene expression, we observed a
192 moderate correlation (Spearman's Rho = 0.159, $p < 2.2e-19$; **Fig. 2d**). Although
193 statistically significant, this modest correlation may be limited because chromatin
194 accessibility does not distinguish between active enhancers and other mechanisms that
195 regulate gene expression. Taken together, these results are consistent with the
196 expectation that increased chromatin contacts are positively associated with gene
197 expression and may contribute to differences in expression across cell types that
198 correlate with clinical phenotypes in POAG.
199
200 **Heritability enrichment of ocular traits in regulatory elements**
201 Next, to determine which traits were enriched in our datasets, we conducted partitioned
202 linkage disequilibrium (LD) score regression to assess enrichment of polygenic signals
203 within genomic annotations across several eye-related traits. We included recent studies
204 on vision-relevant traits, such as myopia and age-related macular degeneration, using
205 publicly available summary statistics from GWAS in European populations. We detected
206 significant enrichments for myopia[62], primary open-angle glaucoma[40], IOP[63], progressive

207 vision loss[64], and macular telangiectasia (**Fig. 3a; Table S2**).[65] For most traits that were
208 enriched in both cell types, the hTMCs displayed stronger enrichment compared to
209 hiPSC-RGCs, except for macular telangiectasia, a retinal disease.[65] We did not detect
210 significant enrichment in retinoschisis.[62] Taken together, these analyses suggest that our
211 datasets can serve as a useful resource for investigating the non-coding contribution of
212 eye-relevant traits.

213 While LD score regression is useful for adjusting for genetic confounding and
214 heritability enrichment, the complexity of long-distance LD has limited its application for
215 recently admixed groups, such as African Americans.[66] Recently, LD score regression
216 has been extended to accommodate these issues in covariate-adjusted LDSC[67], which
217 extends the LD window and uses principal components from the LD matrix as covariates
218 for the regression. We performed partitioned LD score regression using our annotations
219 with our recent African ancestry-based GWAS.[37] While the GWAS sample size is slightly
220 under the threshold for consistent signals used in the UK Biobank, we detected nominal
221 significance with strong enrichment only in hTMCs (hTMC: Enrichment = 17.2,
222 Unadjusted p = 0.044). This result, combined with the significant result in the European
223 POAG study (**Fig.3a**)[40], motivated us to pursue variant-to-gene mapping for genome-wide
224 significant POAG variants.[37]

225

226 **Variant-to-gene mapping of genome-wide significant POAG loci in African ancestry**
227 **individuals**

228 We next took 46 sentinel variants representing independent signals that achieved
229 genome-wide significance in our prior GWAS of POAG in African ancestry indivdiuals.[37]

230 We first expanded to proxy variants in strong linkage disequilibrium (LD; $r^2 > 0.6$) using
231 either the sample matrix or TOPMED-LD[68] and LDLink 1000G reference databases.[69]
232 This yielded 4,438 variants, with ~56% agreement among two or more approaches (**Fig.**
233 **3b**). We then intersected these variants with OCRs showing significant chromatin
234 contacts at a gene promoter, identifying 44 variants in hiPSC-RGCs that collectively
235 interacted with 56 genes. Similarly, 10 variants in hTMCs were in contact with 24 genes
236 (**Table S3**). Among the loci investigated, our approach nominated at least one gene for
237 20 loci (43 % of signals).

238 From this list of putative effector genes, we prioritized variants based on: (1)
239 overlap of findings from our prior orthogonal approaches, such as GWAS, and implication
240 in other genetic studies of POAG (such as the *ARHGEF12* variant), (2) genes involved in
241 neuronal function (*UCHL1, TUBB2B* and its associated lincRNA *LINC02525*), (3) genes
242 involved in other retinal degeneration diseases (*CRB1* and *EXOSC2*), (4) antioxidant
243 gene (*CAT*), (5) molecules involved in key cellular pathways of eye development such as
244 Rho/Rho-associated kinase (ROCK) and Notch signaling pathways (*ARHGEF12*,
245 *ROCK1*, *MIB2*, *MTA1* and its associated lincRNA *AL928654.1*).

246 We analyzed the mRNA expression of the selected genes in hTMCs isolated from
247 human donor control eyes and POAG cases who underwent trabeculectomy. First, we
248 confirmed the authenticity of isolated hTMCs by assessing *myocilin* expression via qRT-
249 PCR, which showed that dexamethasone-treated cells expressed significantly higher
250 *MYOC* than untreated cells (**Fig. S3a-e**).[70] When comparing mRNA expression of genes
251 in hTMCs, we found that *ARHGEF12* (4 ± 0.13, $p = 0.0001$) and *ROCK1* (2.75 ± 0.12, p
252 $= 0.0001$) were significantly elevated in hTMCs obtained from a POAG patient carrying a

253 heterozygous SNP (rs11824032G>A). Similarly, *MIB2* was significantly elevated (1.72 ±
254 0.12, $p = 0.0007$) in POAG hTMCs with a homozygous SNP (rs4320726). However, there
255 was no significant difference in the expression of *CAT* (**Fig. 4a-d**). Genotype information
256 for the variants associated with the tested genes in each hTMC line is listed in **Table S4**.
257 Analysis of mRNA expression of genes in hiPSC-RGCs generated from control
258 and POAG lines carrying the *ARHGEF12* variant showed that *ARHGEF12* was
259 significantly downregulated (0.35 ± 0.05, $p = 0.006$) in the POAG hiPSC-RGCs. Similarly,
260 *TUBB2B* (0.05 ± 0.07, $p < 0.0001$), *LINC02525* (0.015 ± 0.1, $p < 0.0001$), *EXOSC2* (0.48
261 ± 0.07, $p < 0.0001$), *UCHL1* (0.57 ± 0.15, $p = 0.03$), and *CRB1* (0.53 ± 0.15, $p = 0.01$)
262 genes were all significantly downregulated in POAG hiPSC-RGCs compared to control
263 cells. However, there was no significant difference in the expression of *ROCK1* and
264 *MTA1*/ *AL928654.1* (**Fig. 4e-m**). Genotype information for each gene in the hiPSC-RGC
265 lines is listed in **Table S5.**
266

267 **Functional validation of *ARHGEF12* variant in patient-derived hiPSC-RGCs**

268 We initially identified *ARHGEF12* through fine mapping and colocalization analyses.[37]
269 We detected two variants (rs34002948 and rs11824032) corresponding to two
270 independent signals ($r^2 = 0$) with contacts to promoters of this locus in hiPSC-RGCs (**Fig.**
271 **5a**). We predicted transcription factor motifs that could be either strengthened or disrupted
272 by these variants (**Fig. 5b**). rs11824032 was predicted to disrupt several Kruppel-like zinc
273 finger family motifs, while rs34002948 was predicted to strengthen affinity for several
274 nuclear receptor family members. Among these, *KLF1* and *NR1I3* had the strongest
275 expression in hiPSC-RGCs (**Fig. 5c**). The variant rs11824032 was in close proximity to

276 the transcription start site (TSS) (<5kb), whereas the other variant was implicated through
277 a long-distance interaction (~1 Mb) spanning several genes. Indeed, this gene was
278 moderately expressed (TPM =1.57) in control hiPSC-RGCs, leading us to prioritize the
279 *ARHGEF12* gene for functional validation.

280 We confirmed homozygous risk genotype for rs11824032G>A at the *ARHGEF12*
281 gene in a POAAGG subject via Sanger sequencing (**Fig. S4b**) and selected an age- and
282 sex-matched non-risk control (**Fig. S4a**). PBMCs were collected, reprogrammed into
283 hiPSCs, and differentiated into RGCs using our 2D differentiation protocol.[71-73] Day-35
284 FACS analysis showed *ARHGEF12*-variant hiPSC-RGCs expressed BRN3 (87%) and
285 SNCG (92%) (**Fig. S4d**), while control hiPSC-RGCs also expressed BRN3 (96%) and
286 SNCG (92%) (**Fig. S4c**).

287 Using western blot, we observed a trend toward decreased ARHGEF12 protein
288 levels (0.79 ± 0.24) in hiPSC-RGCs derived from the POAG line (n = 3), but this difference
289 was not statistically significant (**Fig. 5d-e**). However, ultrastructural analyses using
290 transmission electron microscopy (TEM) revealed marked morphological differences
291 between control and disease-variant hiPSC-RGCs. Control cells exhibited elongated
292 mitochondria with an outer double membrane, intact cristae, dense matrix, and well-
293 organized cytoplasm consistent with normal metabolic activity, whereas *ARHGEF12*
294 variant cells displayed swollen, vacuolated mitochondria, cytoplasmic disorganization,
295 and accumulation of autophagic vacuoles containing undigested material (**Fig. 5f**).[74]
296 These results highlight variant-linked cellular vulnerability.

297 To investigate the functional effects of the *ARHGEF12* variant on RGC activity,
298 fluorescent Ca^{2+} indicators were used to indirectly measure neuronal responses of

299 hiPSC-RGCs.[75-77] Intracellular calcium dynamics were recorded from hiPSC-RGCs
300 loaded with BioTracker™ 609 Red Ca^{2+} AM dye, and spontaneous activity-driven signals
301 were imaged using a laser-scanning confocal microscope. We analyzed fluorescence
302 responses from more than 200 spontaneously active RGCs from each hiPSC line and
303 observed a range of response dynamics. However, when averaged across all cells,
304 significant differences in fluorescence intensity were detected between the two hiPSC-
305 RGC lines (**Fig. 5g**). Total RGC activity, which was expressed as the summed amplitudes
306 of all Ca^{2+} responses, was 53 ± 1.75% (n = 215) in control hiPSC-RGCs and 28 ± 0.82%
307 (n = 213) in *ARHGEF12* variant-expressing hiPSC-RGCs (**Fig. 5h**). **Videos 5a** and **5b**
308 illustrate representative Ca^{2+} signals in control and *ARHGEF12* variant hiPSC-RGCs,
309 respectively (note that video frame rates were increased for presentation purposes).
310

311 **Discussion:**

312 POAG is highly heritable, yet known genes explain less than 10% of cases[78] and over
313 30% of patients do not respond to current therapies.[79,80] POAG pathogenesis remains
314 unclear; increased resistance to aqueous humor outflow by trabecular meshwork cells
315 leads to elevated intraocular pressure, which causes RGC death and optic nerve
316 degeneration.[81] While GWAS has identified many loci associated with POAG and its
317 phenotypes, most are non-coding with small effects. Here, we aimed to link SNPs to target
318 genes and clarify the role of coding and non-coding variants in POAG. We integrated
319 variants implicated by our large GWAS in overaffected and understudied African ancestry
320 populations with gene expression analysis, accessible chromatin peaks, and 3D
321 chromatin architecture maps in two glaucoma-specific cell types. Together, our analysis

322 implicated 24 genes in hTMCs and 56 genes in hiPSC-RGCs with paired expression from
323 the same donors. These cell-type-specific variant lists will aid in understanding the gene-
324 regulatory networks leading to vision loss in POAG patients.

325 We constructed a network of promoters and candidate cis-regulatory elements by
326 linking promoters to ATAC-seq defined OCRs, providing a resource for investigating
327 GWAS variants in eye-relevant traits. We characterized the interconnected promoters and
328 open chromatin via chromatin contacts, and observed connectivity with many promoters
329 contacting multiple OCRs and OCRs shared across promoters. We demonstrated that
330 regulatory elements in hTMCs and hiPSC-RGCs were enriched for relevant diseases
331 (**Fig. 3a**), with hTMCs showing stronger enrichment for heritability for most traits, which
332 may be due to their role in regulating intraocular pressure while causing the death of
333 RGCs as a consequence. Prior atlases[12,82] were focused exclusively on retinal cell types,
334 highlighting the utility of expanding to other eye cell types to improve understanding of
335 glaucoma etiology. However, these datasets were generated in a single cell state. Future
336 work investigating chromatin conformation in these cells under different relevant
337 conditions, such as oxidative stress and glucocorticoids, is warranted.

338 One of the genes of interest implicated in hiPSC-RGCs and hTMCs was
339 *ARHGEF12*. This gene has been associated with POAG by several orthogonal
340 approaches. Previous GWAS reports revealed an association between the *ARHGEF12*
341 locus and endophenotypes, such as vertical cup-to-disc ratio (CDR) and IOP at the
342 following lead variants: rs58073046[41,51], rs199800298[40], rs2305013[41], and
343 11:120357425.[83] Furthermore, our group previously identified genetic colocalization
344 between the lead variant (rs11824032) mapping to *ARHGEF12* and baseline CDR.[37] Our

345 variant-to-gene mapping results implicated rs11824032 as a putative causal SNP
346 targeting its nearest gene, *ARHGEF12*. In addition, we also detected a long-range
347 promoter contact to rs34002948, a variant associated with the "*TECTA*" locus (**Fig 5a;**
348 **Table S3**). Given this gene's nomination by two independent signals, both local and long-
349 range to the gene-body, we selected *ARHGEF12* for further characterization in hiPSC-
350 RGCs.[41,84]

351 EyeBrowse, an eye-centric genome browser, has shown that *ARHGEF12* is
352 expressed in the TM, retina, and optic nerve.[85] Furthermore, *Arhgef12* transcripts were
353 detected in RGCs at P14 in mice.[86] It is widely reported that ARHGEF12 binds directly to
354 ABCA1 and RhoA/RhoA kinase proteins; the signaling pathway is known to reduce TM
355 plasticity, thereby increasing resistance to aqueous humor outflow and subsequently
356 increasing IOP.[87-89] However, there is very limited knowledge of its functional role in the
357 retina or RGCs. In our study, mRNA analysis of *ARHGEF12* transcripts in hTMCs showed
358 significantly elevated expression, whereas in hiPSC-RGCs, the POAG line showed
359 significantly downregulated expression, representing a truly novel finding. Using western
360 blotting, we observed that POAG hiPSC-RGCs produced lower levels of ARHGEF12
361 protein than control hiPSC-RGCs. Since ARHGEF12 is part of the Rho/ROCK signaling
362 pathway, we also investigated expression of its downstream mediators. We detected a
363 significant overexpression of *ROCK1* transcripts in POAG hTMCs carrying a
364 heterozygous SNP (rs11824032G>A) at the *ARHGEF12* gene. However, there was no
365 significant difference in *ROCK1* expression between control and POAG hiPSC-RGCs.

366 In the context of these findings, we further evaluated RGC pathophysiology in
367 control and POAG hiPSC-RGCs carrying the *ARHGEF12* variant by examining functional

368 activity through calcium imaging. Because Ca^{2+} influx through voltage-gated Ca^{2+}
369 channels are tightly coupled to action potential firing, dynamic intracellular Ca^{2+} changes
370 provide an indirect yet robust measure of neuronal function in hiPSC-RGCs. Calcium
371 imaging revealed pronounced differences in spontaneous activity between control and
372 glaucomatous hiPSC-RGCs. Specifically, fluorescence changes (ΔF/F) were 53 ± 1.75%
373 (*n* = 215) in control cells and 28 ± 0.82% (*n* = 213) in *ARHGEF12* variant–expressing
374 cells. For context, naïve RGCs in wild-type mouse retina exhibit $\Delta F/F_0$ values in the range
375 of ~150–200%[90], underscoring both the reduced responsiveness of hiPSC-RGCs relative
376 to native tissue and the pronounced impairment associated with the *ARHGEF12* variant.
377 We also performed single-cell patch-clamp recordings to directly assess
378 electrophysiological properties in control and variant-expressing hiPSC-RGCs. However,
379 these experiments yielded inconclusive results due to low firing rates and sampling
380 bias.[91-94] Given these limitations, calcium imaging was chosen as a more scalable and
381 reliable method for functional comparison.

382 We also selected other genes implicated in hTMCs from our study for further
383 analysis, such as *CAT* and *MIB2*. TMCs are highly sensitive to oxidative stress; in fact,
384 several studies have reported that the progression of POAG may be due to reduced
385 antioxidant capacity of the TMCs.[95-97] Therefore, the presence of the *CAT* variant, an
386 antioxidant, in our list warranted further investigation. Serum samples collected from
387 patients with POAG have been reported to exhibit low levels of catalase (CAT).[98]
388 However, in our study, we did not detect a significant difference in *CAT* expression
389 between control and POAG hTMCs. Another gene of interest from our hTMC list was the
390 *MIB2* gene, which encodes the E3 ubiquitin protein ligase involved in Notch signaling, a

391 pathway crucial for eye development. Furthermore, the Mouse Genome Informatics
392 database reported that *Mib2-deficient* mice exhibit variable neural tube closure defects
393 and abnormal eye morphology.[99,100] We detected a significant difference in *MIB2*
394 expression between control and POAG hTMCs with a homozygous SNP (rs4320726).

395 Similarly, we investigated the mRNA expression of several genes of interest from
396 our putative list in hiPSC-RGCs, such as *TUBB2B/ LINC02525*, *CRB1*, *EXOSC2*, *UCHL1*,
397 and *MTA1*/ *AL928654.1*. For example, the *TUBB2B* gene (*LINC02525*, its associated
398 lincRNA) encodes ß-tubulin, a crucial building block of neuronal cell structure. Mutations
399 in this gene have been reported to affect neuronal migration and axonal guidance,
400 resulting in severe malformations.[101,102] In our study, *TUBB2B* and *LINC02525* mRNA
401 expression were significantly downregulated in POAG hiPSC-RGCs carrying the
402 *ARHGEF12* SNP. Another group reported that NMDA-mediated excitotoxicity
403 downregulates *ARHGEF12* and *TUBB2B* expression in neurons.[103] Similarly, *UCHL1*,
404 encoding a ubiquitin enzyme, is specifically expressed in neurons and is involved in
405 maintaining synaptic function.[104,105] Its expression was significantly downregulated in
406 POAG hiPSC-RGCs. The expression of *CRB1*[106-113] and *EXOSC2*[114], which are genes
407 with known roles in other retinal degeneration diseases, such as retinitis pigmentosa and
408 Leber congenital amaurosis, was also significantly downregulated. *Arhgef12* is reported
409 to be a modifier gene variant that contributes to *Crb1*-associated retinal dystrophy in
410 mice.[115] In the case of *MTA1*/ *AL928654.1*, we detected contacts between rs187398392
411 and the *Metastasis-associated 1* (*MTA1)* gene and associated lncRNA
412 (*AL928654.1*/*MTA1-DT*), which are both established cancer genes. While *MTA1* has not
413 been implicated in POAG, it has a known role in retinal development through interactions

414 with SIX3, which regulates the number of retinal cells during development.[116] In this study,
415 we did not detect a significant difference in *MTA1* and *AL928654.1* expression between
416 control and POAG hiPSC-RGCs.

417 This study focused on the *ARHGEF12* variant rs11824032, so hiPSCs were
418 generated only from POAG subjects with or without the risk allele, without controlling for
419 other variants. To address this, we are combining hiPSC-RGCs with CRISPR/Cas9 to
420 assess mutation-specific effects. Using prime editing, we aim to create isogenic hiPSC
421 lines with a single genetic background. Current editing efficiency for rs11824032G>A is
422 ~30% in HEK293T cells (**Fig. S5**), which we will extend to hiPSCs.

423 In conclusion, we sought to identify SNP-to-gene relationships and to elucidate
424 how variants contribute to POAG pathogenesis. By integrating LD-expanded variants with
425 ATAC-seq and Hi-C data, we implicated 24 genes in hTMCs and 56 in hiPSC-RGCs,
426 including *ARHGEF12*, which was identified in our prior GWAS. qRT-PCR confirmed
427 differential *ARHGEF12* expression between POAG and controls, and variant-carrying
428 hiPSC-RGCs showed altered light-evoked responses. This extensive variant-to-gene
429 dataset will serve as a key resource to the POAG research community going forward.

430

431 **Limitations**: The hiPSC-RGC analysis of the *ARHGEF12* variant is preliminary, as we
432 did not investigate how the variant affects RGC function. Ca^{2+} results should also be
433 interpreted cautiously, since high-intensity, prolonged light stimulation may introduce
434 artifacts. Additionally, we measured only intracellular calcium, not the electrical activity of
435 RGCs.

436 POAG is a complex polygenic disease. To assess its heterogeneous
437 pathogenicity, pooled CRISPR screens could be used to introduce gRNA libraries into
438 hiPSCs, enabling gene overexpression or knockout.[117] These cells can then be
439 differentiated into RGCs, and sequencing of integrated gRNAs may reveal genes involved
440 in RGC function and POAG pathogenesis.
441
442 **Materials and Methods:**
443
444 **Human iPSC culture**
445 Undifferentiated hiPSCs were generated and characterized at the University of
446 Pennsylvania iPSC Core Facility, providing a comprehensive analysis of hiPSC
447 characteristics.[118-120] The University of Pennsylvania and the Children's Hospital of
448 Philadelphia Human Subjects Research Institutional Review Boards approved all human
449 sample collection protocols consistent with the Declaration of Helsinki. All methods were
450 performed in accordance with the University of Pennsylvania's relevant research
451 guidelines and regulations. Written informed consent was obtained from all human cell
452 donors. The hiPSCs were maintained in StemMACs iPSC-Brew XF (Miltenyi Biotec,
453 catalog #: 130-107-086, North Rhine-Westphalia, Germany) containing 50X supplement
454 (Miltenyi Biotec, catalog #: 130-107-087, North Rhine-Westphalia, Germany), and Pen
455 Strep (Life Technologies, catalog #: 10378-016, Carlsbad, CA, USA). Demographics of
456 the POAAGG subjects from whom the hiPSCs were generated are listed in **Table S6**.
457
458

459 **Retinal progenitor cell (RPC) generation and conditions**

460 hiPSCs were cultured on Matrigel-coated plates (Corning, catalog #: 354230, Corning,
461 NY, USA) in 37°C, 5% O_2, and 5% CO_2 conditions. Cells were maintained until they
462 reached 75% confluency. hiPSCs were then split and seeded in one well of a 6-well tissue
463 culture dish (Corning, catalog #: 229106, Corning, NY, USA) coated with 1:100 diluted
464 Matrigel growth factor. hiPSCs were maintained at 37 °C, 5% O_2, and 5% CO_2 until
465 reaching 100% confluence then transferred to 37 °C, 5% CO_2 overnight prior to induction.
466 On day 0, iPSC-Brew media was changed to RPC induction media: DMEM/F12 (50:50;
467 Corning, catalog #: 10-092-cm, Corning, NY, USA), 1% Pen Strep (Life Technologies,
468 catalog #: 10378-016, Carlsbad, CA, USA), 1% Glutamine MAX (Life Technologies,
469 catalog #: 35050-061, Carlsbad, CA, USA), 1% NEAA (Life Technologies, catalog #:
470 11140-050, Carlsbad, CA, USA), 0.1 mM 2-ME (Life Technologies, catalog #: 21985-023,
471 Carlsbad, CA, USA), 2% B27 supplement (w/o vitamin A; Life Technologies, catalog #:
472 12587-010, Carlsbad, CA, USA), 1% N2 supplement (Life Technologies, catalog #:
473 17502-048, Carlsbad, CA, USA), containing 2 μM XAV939 (X) (Wnt inhibitor; R&D
474 Systems, catalog #: 3748, Minneapolis, MN, USA), 10 μM SB431542 (SB) (TGF-β
475 inhibitor; R&D Systems, catalog #: 1614, Minneapolis, MN, USA), 100 nM LDN193189
476 (L) (BMP inhibitor; R&D Systems, catalog #: 6053, Minneapolis, MN, USA), 10 mM
477 nicotinamide (Sigma-Aldrich, catalog #: N0636, St. Louis, MO, USA), and 10 ng/mL IGF1
478 (R&D Systems, catalog #: 291-G1, Minneapolis, MN, USA). Cultures were fed daily for
479 4 days. On day 4, the culture medium was exchanged for RPC induction media containing
480 2 μM XAV939, 10 μM SB431542, 100 nM LDN193189, 10 ng/mL IGF-1, and 10 ng/mL
481 bFGF. The media was changed daily for 21 days.[73]

482 **RGC differentiation**

483 Before RGC differentiation, the medium was changed daily using iNS media containing
484 250 ng/mL Shh (R&D Systems, catalog #: 8908-SH, Minneapolis, MN, USA), 100 ng/mL
485 FGF8 (R&D Systems, catalog #: 423-F8, Minneapolis, MN, USA) for 2 days. For RGC
486 differentiation on day 24, cells were manually crossed into small clusters with Leibovitz's
487 medium containing 34 μM D-Glucose (Research Products International, catalog #:
488 G32045-500, Mt. Prospect, IL, USA) using the crosshatching technique as previously
489 described[121], then re-plated at a density of 1.0×10^5 cells/well of 6-well plate coated with
490 1:100 diluted Matrigel growth factor in RGCs induction media containing: 100 ng/mL
491 Follistatin 300 (R&D Systems, catalog #: 669-FO, Minneapolis, MN, USA), 0.5 μM
492 Cyclopamine (R&D Systems, catalog #: 1623/1, Minneapolis, MN, USA), 3 μM DAPT
493 (Stemgent, catalog #: 04-0041, Cambridge, MA, USA), and 4.2 μM Y-27632
494 dihydrochloride (Rock inhibitor; R&D Systems, catalog #: 1254/1, Minneapolis, MN, USA).
495 The media was changed 24 hours post-plating with RGC induction media containing
496 100 ng/mL Follistatin 300 and 3 μM DAPT daily for 2 days. From day 27, media was
497 changed to RGC induction media containing: 3 μM DAPT, 10 μM Rock inhibitor (Y27632),
498 5 μM Forskolin (Selleckchem, catalog #: S2449, Houston, TX, USA), 400 μM N^6,2′-O-
499 Dibutyryladenosine 3′,5′- cyclic monophosphate sodium salt (cAMP; Sigma-Aldrich,
500 catalog #: D0627, St. Louis, MO, USA), 40 ng/mL BDNF (R&D Systems, catalog #: 248-
501 BDB, Minneapolis, MN, USA), 5 ng/mL NT4 (R&D systems, catalog #: 268-N4,
502 Minneapolis, MN, USA), and 10 ng/mL CNTF (R&D systems, catalog #: 257-NT,
503 Minneapolis, MN, USA). The media was changed every 2-3 days until day 36. After

504 maturation (D36), the medium was exchanged every 3-4 days with RGC induction media
505 containing 3 μM DAPT and 10 μM Rock inhibitor (Y27632).[73]
506
507 **hTMCs**
508 For the 3D genomic experiments, such as RNA-seq, ATAC-seq, and Hi-C, Primary
509 trabecular meshwork cells were used, which were commercially obtained (ScienCell,
510 catalog #: 6590, Carlsbad, CA, USA).
511 For the functional validation of the variants, hTM tissue strips were isolated either
512 from whole globes or obtained from glaucoma patients during trabeculectomy surgery at
513 the Scheie Eye Institute. hTM tissues isolated from post-mortem donor eyes were
514 obtained from the National Disease Research Interchange (NDRI). Whole globes were
515 bisected near the equator, and the iris, lens, and ciliary processes were gently removed
516 from the anterior segment. The anterior segment was then divided into two half-wedges.
517 Using fine-tipped forceps, hTM tissue was grasped at the cut edge of each wedge and
518 gently pulled away. Each hTM strip was cut into three pieces. hTM tissue from whole
519 globes and trabeculectomy (typically 0.5–1 mm) was incubated for 30 minutes in DMEM
520 (Gibco, catalog #: 11885-084, Waltham, MA, USA) containing 10 mg/mL dispase (Gibco,
521 catalog #: 17105-041, Waltham, MA, USA) and 10 mg/mL collagenase (Gibco, catalog #:
522 17104-019, Waltham, MA, USA) at 37°C. Tissues were washed once with DMEM, then
523 placed onto gelatin-coated plates with coverslips. hTM pieces from whole globes were
524 distributed into three wells of a 6-well plate, while surgical hTM tissue was placed in one
525 well. Coverslips were positioned to secure the tissue, and DMEM supplemented with 10–
526 20% FBS (Cytiva Hyclone, catalog #: SH30910.03, Logan, UT, USA) and penicillin-

527 streptomycin (Gibco, catalog #: 15140-122, Waltham, MA, USA) was applied. Culture
528 media was replaced every five days. Once the hTMCs reached confluence. Cultures were
529 expanded further as needed or cryopreserved for long-term storage.[70]

530 We validated the authenticity of the hTMCs by performing *MYOC* induction
531 experiments with 100 nM dexamethasone (Sigma-Aldrich, catalog #: D4902, St. Louis,
532 MO, USA), freshly added to the media every 2–3 days for two weeks, which significantly
533 increased *MYOC* expression by qRT-PCR relative to untreated controls.[70] For all our
534 experiments, we used primary TM cultures from Passage 2 (P2) to Passage 4 (P4).
535 Demographics of the patients from whom the hTMCs were isolated are listed in **Table**
536 **S7**.

537

538 **Sanger sequencing**

539 DNA was extracted from hTMCs, control, and *ARHGEF12* disease-variant hiPSC-RGCs
540 using the Purelink genomic DNA mini kit (Invitrogen, catalog #: K1820-01, Waltham, MA,
541 USA). DNA was quantified using the Qubit dsDNA BR assay kit (Invitrogen, catalog #:
542 Q32853, Waltham, MA, USA) and Qubit 2.0 fluorometer. PCR was performed using the
543 GoTag Green Master Mix (Promega, catalog #: M7122, Madison, WI, USA), and the
544 primer sets are listed in **Table S8**. PCR products were purified using Gel and PCR
545 cleanup kit (Macherey-Nagel, catalog #: 74069.250, Düren, Germany) and submitted for
546 Sanger sequencing at the Penn Genomic and Sequencing Core. Sequencing data were
547 analyzed using NCBI BLAST and the UGENE (Unipro) software.

548

549

550 **ATAC-seq in hTMCs and hiPSC-RGCs**

551 A total of 50,000 to 100,000 cells were centrifuged at 500 xg for 5 min at 4°C. The cell
552 pellet was washed with cold PBS and resuspended in 50 µL of cold lysis buffer (10 mM
553 Tris-HCl, pH 7.4, 10 mM NaCl, 3 mM MgCl2, 0.1% NP-40/IGEPAL CA630) and
554 immediately centrifuged at 550 xg for 10 min at 4°C. Nuclei were resuspended in the
555 Nextera transposition reaction mix (25 µL 2x TD Buffer, 2.5 µL Nextera Tn5 transposase
556 (Illumina, USA Cat #FC-121-1030), and 22.5 µL nuclease-free H2O) on ice, then
557 incubated for 45 min at 37°C. The tagmented DNA was then purified using the Qiagen
558 MinElute kit, eluted with 10.5 µL Elution Buffer (EB). Ten microliters of purified tagmented
559 DNA were PCR amplified using Nextera primers for 12 cycles to generate each library.
560 The PCR reaction was subsequently cleaned up using 1.5x AMPureXP beads
561 (Agencourt, Beverly, MA, USA), and concentrations were measured by Qubit. Libraries
562 were paired-end sequenced using an Illumina NovaSeq 6000 (CHOP 51 bp read length).

563 Image files were demultiplexed using bcf2fastq (v2.20.0, Illumina, San Diego, CA,
564 USA). Briefly, pair-end reads from three biological replicates for each cell type were
565 aligned to hg38 genome using bowtie2,[122] and duplicate reads were removed from the
566 alignment. Narrow peaks were called independently for each replicate using macs2 (-p
567 0.01 --nomodel --shift -75 --extsize 150 -B --SPMR --keep-dup all -callsummits),[123] and
568 ENCODE blacklist regions were removed from peaks in individual replicates. The
569 reproducible peak set (ATAC-seq peaks called by MACS peaks called with q-value <
570 0.01) was used as the consensus OCRs for each cell type. ATAC-seq fragment
571 distribution plots were generated using the fragSizeDist function from the Bioconductor
572 package ATACseqQC (v 1.28.0)[124] with the deduplicated bam files.

573 **Hi-C in hiPS-RGC**

574 For the hiPS-RGCs, Hi-C libraries were prepared for two biological replicates using the
575 Arima-HiC kit (Arima Genomics, catalog #: A410030, Carlsbad, CA, USA), according to
576 the manufacturer's protocols. Briefly, cells were crosslinked using formaldehyde.
577 Crosslinked cells were then subject to the Arima-HiC protocol, which utilizes multiple
578 restriction enzymes (targeting ^GATC and G^ANTC) to digest chromatin. Arima-HiC
579 sequencing libraries were prepared by first shearing purified proximally ligated DNA and
580 then size-selecting 200–600 bp DNA fragments using AmpureXP beads (Beckman
581 Coulter, catalog #: A63882, Brea, California, USA). The size-selected fragments were
582 then enriched using Enrichment Beads (provided in the Arima-HiC kit) and then converted
583 into Illumina-compatible sequencing libraries with the Swift Accel-NGS 2S Plus DNA
584 Library Kit (Swift, catalog #: 21024, Ann Arbor, MI, USA) and Swift 2S Indexing Kit (Swift,
585 catalog #: 26148, Ann Arbor, MI, USA). The purified, PCR-amplified DNA underwent
586 standard QC (qPCR, Bioanalyzer, and KAPA Library Quantification (Roche, catalog #:
587 KK4824, Basel, Switzerland)) and was sequenced with unique single indexes on the
588 Illumina NovaSeq 6000 Sequencing System at 2x51 base pairs. For these biological
589 replicates, two technical replicates were performed to fill the appropriate S4 flow cell.

590

591 **Promoter Capture C in hTMCs**

592 For the hTM library, 107 fixed cells were thawed at 37ºC, followed by centrifugation at RT
593 for 5 mins at 1845 xg. The cell pellet was resuspended in 1 mL of dH2O supplemented
594 with 5 µL 200X protease inhibitor cocktail, incubated on ice for 10 minutes, and then
595 centrifuged. Cell pellet was resuspended to a total volume of 650 µL in dH2O. 50 µL of

596 cell suspension was set aside for pre-digestion QC, and the remaining sample was
597 divided into 3 tubes. Both pre-digestion controls and samples underwent a pre-digestion
598 incubation in a Thermomixer (BenchMark, Tempe, AZ, USA) with the addition of 0.3%
599 SDS, 1x NEB DpnII restriction buffer, and dH_2O for 1 hour at 37ºC, shaking at 1,000 rpm.
600 A 1.7% solution of Triton X-100 was added to each tube, and shaking was continued for
601 another hour. After pre-digestion incubation, 10 µL of DpnII (NEB, 50 U/µL) was added
602 to each sample tube only and continued shaking along with pre-digestion control until the
603 end of the day. An additional 10 µL of DpnII was added to each digestion reaction, and
604 the mixture was digested overnight. The next day, an additional 10 µL of DpnII was added,
605 and the mixture continued to shake for another 2-3 hours. 100 uL of each digestion
606 reaction was then removed, pooled into one 1.5 mL tube, and set aside for digestion
607 efficiency QC. The remaining samples were heat-inactivated by incubating at 1000 rpm
608 in a MultiTherm for 20 minutes at 65°C to inactivate the DpnII, followed by cooling on ice
609 for an additional 20 minutes. Digested samples were ligated with 8 uL of T4 DNA ligase
610 (HC ThermoFisher, 30 U/µL) and 1X ligase buffer at 1,000 rpm overnight at 16°C in a
611 MultiTherm.

612 The next day, an additional 2 µL of T4 DNA ligase was spiked into each sample
613 and incubated for another few hours. The ligated samples were then de-crosslinked
614 overnight at 65°C with Proteinase K (20 mg/mL; Denville Scientific, Holliston, MA, USA)
615 along with pre-digestion and digestion control. The following morning, both controls and
616 ligated samples were incubated for 30 min at 37°C with RNase A (Millipore, Burlington,
617 MA, USA), followed by phenol/chloroform extraction, ethanol precipitation at -20°C, the
618 3C libraries were centrifuged at 1000 xg for 45 min at 4°C to pellet the samples. The

619 controls were centrifuged at 1845 xg. The pellets were resuspended in 70% ethanol and
620 centrifuged as described above. The pellets of 3C libraries and controls were
621 resuspended in 300 µL and 20 µL dH2O, respectively, and stored at −20°C. Sample
622 concentrations were measured by Qubit. Digestion and ligation efficiencies were
623 assessed by gel electrophoresis on a 0.9% agarose gel and by quantitative PCR (SYBR
624 green; Thermo Fisher, Waltham, MA, USA).

625 Isolated DNA from 3C libraries was quantified using a Qubit fluorometer (Life
626 Technologies, Carlsbad, CA, USA), and 10 µg of each library was sheared in dH_2O using
627 a QSonica Q800R to an average fragment size of 350bp. The QSonica settings used
628 were 60% amplitude, 30 seconds on, 30 seconds off, with 2-minute intervals, for a total
629 of 5 intervals at 4°C. After shearing, DNA was purified using AMPureXP beads
630 (Agencourt, Beverly, MA, USA). DNA size was assessed using a Bioanalyzer 2100 with
631 a DNA 1000 Chip (Agilent, Santa Clara, CA, USA), and DNA concentration was
632 determined via Qubit. SureSelect XT library prep kits (Agilent, Santa Clara, CA, USA)
633 were used to repair DNA ends and for adaptor ligation following the manufacturer's
634 protocol. Excess adaptors were removed using AMPureXP beads. Size and
635 concentration were verified using a Bioanalyzer with a DNA 1000 Chip and a Qubit
636 fluorometer before hybridization. One microgram of adaptor-ligated library was used as
637 input for the SureSelect XT capture kit using the manufacturer's protocol and our custom-
638 designed 41K promoter Capture-C library. The quantity and quality of the captured library
639 were assessed using a Bioanalyzer with a high-sensitivity DNA Chip and a Qubit
640 fluorometer. SureSelect XT libraries were then paired-end sequenced on the Illumina
641 NovaSeq 6000 platform (CHOP; 51 bp read length).

642 Hi-C and Promoter Capture C data were processed using the HiCUP pipeline
643 (v0.7.4).[125] Significant chromatin contacts were called with Chicago (Score > 5)[57] for
644 Promoter-focused Capture C data (Chicago Score > 5), and used the combination of
645 Mustache (FDR < 0.1)[58] and FitHiC2 (FDR < 1x10-6)[59] as performed previously.[6,24]
646
647 **RNA-seq in hTMCs and hiPSC-RGCs**
648 RNA was isolated from ~ 1 million of each cell type using Trizol Reagent (Invitrogen,
649 Waltham, MA, USA), purified using the Directzol RNA Miniprep Kit (Zymo Research,
650 Irvine, CA, USA), and depleted of contaminating genomic DNA using DNAse I. Purified
651 RNA was checked for quality on a Bioanalyzer 2100 using the Nano RNA Chip, and
652 samples with RIN > 7 were used for RNA-seq library preparation. RNA samples were
653 depleted of rRNA using QIAseq Fastselect RNA removal kit (Qiagen, Hilden, Germany).
654 Samples were then processed for library preparation using the SMARTer Stranded Total
655 RNA Sample Prep Kit (Takara Bio, Kusatsu, Shiga, Japan) according to the
656 manufacturer's instructions. Briefly, the purified first-strand cDNA is amplified into RNA-
657 seq libraries using SeqAmp DNA Polymerase and the Forward and Reverse PCR Primers
658 from the Illumina Indexing Primer Set HT for Illumina. The quality and quantity of the
659 libraries were assessed using the Agilent 2100 Bioanalyzer system and Qubit fluorometer
660 (Life Technologies, Carlsbad, California, USA). Sequencing of the finalized libraries was
661 performed on the NovaSeq 6000 platform at the CHOP Center for Spatial and Functional
662 Genomics.

663 RNA-seq was processed using the STAR (v 2.7.9a) pipeline, aligned to hg38 with
664 gencode V30 as the reference. Reads were counted using HTSeq (v2.0.2)[126], and TPM
665 values were calculated using the effective gene length.
666 Differential expression analysis was conducted using standard procedures in the
667 edgeR framework.[127] First gene counts were aggregated across technical replicates.
668 Low-expressed genes were then filtered using the filterByExpr function with the default
669 parameters. Normalization was performed with the trimmed-median of the means method
670 implemented in calcNormFactors. Dispersions were estimated with replicate cell types as
671 a group and parameter robust = TRUE. The model of 0 ~ cell type was fitted using
672 glmQLFit with parameter robust = TRUE and tested with glmQFLTest across the cell type
673 contrast. P-values were adjusted using the Benjamini-Hochberg procedure. Given the
674 extreme differences observed between cell types, we opted for a strict cutoff of
675 abs(logFC) > 7 and FDR < 1e-6 to focus on the strongest differential marker genes. TPM
676 values were calculated as previously described using the effect-gene length.[128] Pathway
677 enrichment was conducted using the hypergeometric test implemented in phyper in R (R
678 Core Team, 2025).
679
680 **LD Score Regression**
681 We checked our chromatin annotations for GWAS heritability enrichment using LD-score
682 regression implemented in LDSC.[129] Publicly available EUR summary statistics were
683 processed using the munge_sumstats.py script provided with ldsc
684 (https://github.com/bulik/ldsc). Annotation files were constructed using open chromatin
685 regions defined for hTMCs or hiPSC-RGCs. For European GWAS studies, LD score

686 regression (v 1.01)[129,130] was run using the European 1000 Genomes Phase3 reference
687 data and developer-provided baseline v2.2 reference files.[131] Enrichment analyses were
688 run with the default parameters, with the exception of –print-coefficients set. Tests were
689 adjusted with Bonferroni correction and false discovery rate (FDR) using the R function
690 p-adjust. Dot plots were generated using the ggplot2 package (v. 4.0.1). For AFR ancestry
691 analyses, covariate-adjusted LD score regression[67] was used to adjust enrichment
692 estimates for recent admix ancestry by incorporating principal components calculated and
693 using an expanded LD window. To construct the reference, the hg38 1000G plink
694 reference files were retrieved from the plink website. Principal components were
695 computed using the eigenstrat smartpca function[132] with the default parameters except
696 numoutevac: 10. These were used in conjunction with the bed file for the 52 binary
697 baseline annotations, as well as hTMC and hiPSC-RGCs as above, to build annotations
698 with --ld-wind-cm set to 20 as previously described.[67] This was used as the annotation to
699 calculate enrichment as above.
700
701 **Genomic Analyses**
702 Comparative analyses for promoter contacts: TPM values were correlated with the
703 number of promoter-connected OCRs using the Spearman correlation coefficient,
704 implemented in the cor.test function with method="speaman" from R (v4.4.0).
705
706 SNP selection and LD expansion: Sentinel SNPs were collected from our previous African
707 ancestry GWAS.[37] These were expanded to any SNPs in high LD ($R^2 > 0.6$) with the

708 signal from the LD matrix of the population, or the EUR/AFR variants from the 1000
709 genomes high coverage set from LDLink[68] or TOPMED-LD.[69]
710
711 Variant to gene mapping: Using the expanded set of genome-wide significant GWAS
712 sentinels and their proxy variants, we intersected variants with the set of OCRs that either
713 overlapped known promoter regions (−1500/+ 500 bp of gencode V30 TSS) or OCR
714 overlapping promoter interacting regions identified by Capture C/ Hi-C in either hiPSC-
715 RGCs or hTMCs. Genomic coordinate overlaps were identified using the R package
716 GenomicRanges (ver 1.56.2)[133] against the hg38 genome reference.
717
718 Transcription factor motif disruption: We used motifbreakR (v.2.19.5)[134] to predict
719 transcription factors that may have disrupted binding by the highlighted variants
720 (rs11824032, rs34002948, rs187398392). Position weight matrices from hocomoco
721 v10[135] were queried against the hg38 genome with the reference and alternative allele.
722 Motifs with strong disruption were predicted using the motifBreakR function, with
723 parameters: filterp = TRUE, threshold = 1e-3, method = "ic", bkg = c(A=0.25, C=0.25,
724 G=0.25, T=0.25), and BPPARAM=BiocParallel::bpparam(). P-values were calculated
725 with the calculatePvalue() function. The TPM-adjusted expression values were then
726 plotted to identify which of the putative regulators may act in hiPSC-RGCs.
727
728 **FACS analysis**
729 hiPSC-RGC cultures were lifted using TrypLE Express (Invitrogen, catalog #: 12605-010,
730 Waltham, MA, USA) and collected by centrifugation at 1600 rpm for 5 minutes at 4 °C.

731 The pelleted cells were resuspended in 1X PBS supplemented with 0.5% bovine serum
732 albumin and 0.1% sodium azide (FACS buffer). Cells were fixed in 4% paraformaldehyde
733 (v/v) for 15 min at room temperature (RT), followed by permeabilization using 0.5%
734 Tween-20 (v/v) for 10 min at RT. Cells were incubated with anti-BRN3 Alexa Fluor 594
735 (Santa Cruz, catalog #: sc-390780, Santa Cruz, CA, USA) and anti-SNCG Alexa Fluor
736 488 (Santa Cruz, catalog #: sc-65979, Santa Cruz, CA, USA). Stained cells were
737 analyzed using LSRFortessa B in the Penn Cytomics and Cell Sorting Shared Resource
738 Laboratory at the University of Pennsylvania (RRID:SCR_022376). The data were further
739 analyzed using FACS software (FlowJo 10.8.1, Ashland, OR, USA).
740
741 **qRT-PCR**
742 Total RNA was extracted from hTMCs and hiPSC-RGCs using RNeasy® Mini Kit
743 (Qiagen, catalog #: 74104, Hilden, Germany). For each sample, 150 ng of total RNA was
744 reverse transcribed using the SuperScript® III first-strand cDNA synthesis kit (Invitrogen,
745 catalog #: 18080-051, Waltham, MA, USA). Amplified cDNA was quantified using Fast
746 SYBR™ Green Master Mix (Applied Biosystems, catalog #: 4385612, Foster City, CA,
747 USA) on a QuantStudio 6 Pro (Applied Biosystems, Foster City, CA, USA), and the primer
748 sets are listed in **Table S9**. All results were normalized to *GAPDH* housekeeping control
749 and were from three technical replicates for each experimental condition. The relative
750 gene expression was compared to that of control cells to obtain normalized gene
751 expression, which is represented as the mean ± SEM.
752
753

754 **Western blot**

755 hiPSC-RGCs from control and *ARHGEF12*-variant lines were scraped off the dish and
756 centrifuged at 1600 rpm for 5 minutes. The pellet was extracted using RIPA buffer (Cell
757 Signaling, catalog #: 9806S, Danvers, MA, USA), which contained protease and
758 phosphatase inhibitors (Roche, catalog #: 03115828001, Mannheim, Germany). Cells
759 were sonicated (15 s X 3) and then incubated on ice for 20 minutes. After lysing the cells,
760 cell debris was removed by centrifugation at 20,000 xg for 30 minutes, and the
761 supernatant containing the cytoplasmic extract was transferred to a new tube. The protein
762 content of the cell lysates was determined using the Qubit protein assay (Invitrogen,
763 catalog #: Q33221, Waltham, MA, USA) with the Qubit 2.0 fluorometer and then
764 normalized to ensure equal protein content. Protein extracts were analyzed using SDS-
765 polyacrylamide gel electrophoresis with Mini-Protean precast gels (Bio-Rad, catalog #:
766 4561094, Hercules, CA, USA) and followed by a western blot. The samples were
767 analyzed for ARHGEF12 protein (Life Technologies, catalog #: PA5143957, Carlsbad,
768 CA, USA), and β-actin (Santa Cruz Biotechnology, catalog #: sc-47778, Santa Cruz, CA,
769 USA) was used as the loading control. The experiments were repeated at least three
770 times.

771

772 **Transmission electron microscopy (TEM)**

773 hiPSC-RGCs from a healthy control line and a POAG-associated *ARHGEF12*-variant line
774 were cultured on 14-mm glass coverslips placed in a standard 24-well plate. Cells were
775 plated at a density of 1×10^5 cells per well to achieve a uniform monolayer suitable for

776 ultrastructural analysis. Cells were maintained under RGC differentiation conditions until
777 they formed a healthy monolayer suitable for ultrastructural analysis.
778 Cells grown on coverslips were fixed with 0.1 M sodium cacodylate buffer (pH 7.4)
779 containing 2.5% glutaraldehyde and 2.0% paraformaldehyde and incubated overnight at
780 4 °C. After thorough buffer washes, samples were post-fixed in 2.0% osmium tetroxide
781 containing 1.5% potassium ferricyanide ($K_3Fe(CN)_6$) for 1 hour at room temperature,
782 followed by rinsing with deionized water. En bloc staining was performed using 2%
783 aqueous uranyl acetate.
784 The samples were then dehydrated through a graded ethanol series, infiltrated,
785 and embedded in EMbed-812 resin (Electron Microscopy Sciences, Fort Washington,
786 PA). Ultrathin sections were stained with uranyl acetate and Sato lead stain and examined
787 using a Talos L120C transmission electron microscope equipped with a Ceta 16 M digital
788 camera.
789
790 **Calcium imaging**
791 Intracellular calcium within live hiPSC-RGCs was stained using BioTracker™ 609 Red
792 Ca2+ AM Dye (Sigma-Aldrich, catalog #: SCT021, St. Louis, MO, USA). 8 µL of the dye
793 (80 µM) was diluted in 902 µL of 1X PBS, along with 10 µL of Pluronic® F-127 (Sigma-
794 Aldrich, catalog # 9003-11-6, St. Louis, MO, USA) and 80 µL of DMSO. hiPSC-RGCs
795 were incubated with the diluted dye for 40 minutes at 37 °C. Images of cells were acquired
796 using an Olympus Fluoview 1000 confocal laser-scanning microscope equipped with an
797 Olympus XLPlan N at 25X magnification. Images were acquired at a resolution of 256 x
798 256 pixels, at ~2 frames per second, and covered an area of 509 × 509 µm. During

799 imaging, cells were continuously perfused with Ames' medium equilibrated with a 5% CO_2
800 / 95% O_2 gas mixture and maintained at 35 °C. Imaging parameters were optimized to
801 capture large fields of view and monitor the activity of as many cells as possible, which
802 necessarily resulted in slower scan rates (approximately 2 frames per second). Under
803 these conditions, individual action potential-evoked Ca^{2+} transients cannot be temporally
804 resolved; instead, firing activity is represented as a normalized fluorescence change
805 (ΔF/F), where ΔF reflects the increase in fluorescence associated with action potential-
806 evoked Ca^{2+} influx and, for short bursts of firing, with spike rate and spike number,
807 population-average ΔF/F provides a useful metric for comparing functional activity across
808 cell types. Fluorescence responses in somas and dendrites were calculated with custom,
809 ScanImage-compatible algorithms in Matlab. Fluorescent structures were outlined by
810 hand using the roipoly function (Signal Processing Toolbox; The MathWorks). The
811 fluorescence intensity of a neuron is reported throughout as the average intensity of all
812 pixels over its soma, including the nucleus. Data was analyzed with custom software
813 (Matlab; The MathWorks). The mean time-dependent fluorescent signal from each RGC
814 (*F*) was normalized by subtracting the mean pre-stimulus signal intensity *(F0)*, which is
815 expressed as $\Delta F = F - F0$. The normalized neuronal responses ($\Delta F/F0$) for each RGC
816 were then calculated.[90,136]
817
818 **Prime editing**
819 Plasmid Constructs and Cloning: The pCMV-PEmax-P2A-GFP (Addgene plasmid #
820 180020) prime editor was used.[137] pegRNA and nsgRNA's were cloned into the pU6-
821 tevopreq1-GG-acceptor (Addgene plasmid # 174038), using BsaI Golden Gate

822 assembly (NEB).[138] All oligos were ordered from Integrated DNA Technologies (IDT).
823 pU6-Sp-pegRNA-ARHGEF12: pegRNA spacer, top strand oligonucleotide:
824 5'-CACCGTCTGATCTCCTCAGAGACTAGTTTC-3'; bottom strand oligonucleotide:
825 5'-CTCTGAAACTAGTCTCTGAGGAGATCAGAC-3' and Installation 3'-extension, top
826 strand oligonucleotide: 5'-GTCCTCCCACTGCATCCCTAGTCTCTGAGGAGAT-3';
827 bottom strand oligonucleotide:
828 5'-CGCGATCTCCTCAGAGACTAGGGATGCAGTGGGA-3'. pU6-ARHGEF12-nsgRNA-
829 1: nsgRNA spacer 1, top strand oligonucleotide:
830 5'-CACCGCCTCCTCTGGGCTCCTCCTCGTTTC-3'; bottom strand oligonucleotide:
831 5'-CTCTGAAACGAGGAGGAGCCCAGAGGAGGC-3'. pU6-ARHGEF12-nsgRNA-2:
832 nsgRNA spacer 2, top strand oligonucleotide:
833 5'-CACCGTCTTCTCACAGGCATCTCTGGTTTC-3'; bottom strand oligonucleotide:
834 5'-CTCTGAAACCAGAGATGCCTGTGAGAAGAC-3'. nsgRNA termination, top strand
835 oligonucleotide: 5'-GTCCTTTTTTTTCGCGGTTCTATCTAG-3'; bottom strand
836 oligonucleotide: 5'-CGCGCTAGATAGAACCGCGAAAAAAAA-3', this is used in place of
837 pegRNA 3'-extension when making nsgRNA using pU6-tevopreq1-GG-acceptor.
838 Scaffold, top strand oligonucleotide:
839 5'-AGAGCTAAGAAATTAGCAAGTTGAAATAAGGCTAGTCCGTTATCAACTTGAAAAA
840 GTGGGACCGAGTCG-3'; bottom strand oligonucleotide:
841 5'-GGACCGACTCGGTCCCACTTTTTCAAGTTGATAACGGACTAGCCTTATTTCAACT
842 TGCTAATTTCTTAG-3'.

843 <u>Cell culture and transfection of HEK293T cells</u>: This was performed as previously
844 described.[139] HEK293T cells were cultured in DMEM (Thermo Fisher Scientific)

845 supplemented with 10% FBS. HEK239T cells were seeded, one day prior to transfection,
846 at 50000 cells/well in 24 well plate. The plasmid constitution for transfection is
847 1050ng:393.75ng:78.75ng of CMV-PEmax: U6-pegRNA: U6-ngRNA. Lipofectamine
848 2000 (Thermo Fisher) and plasmid DNA were mixed at a 1:1 mass ratio. Cells were
849 collected 72 hours post transfection for DNA extraction and analysis.

850 DNA extraction: This was performed as previously described.[140] HEK293T cells were
851 detached with trypsin, DPBS washed, and finally re-suspended in 30 µl of DPBS.
852 HEK293T cells were subsequently incubated at 95°C for 20 mins, 4ul of 20mg/ml
853 Proteinase K (Promega) was added, and a further incubation at 56°C for 1h followed by
854 a final 30 min incubation at 95°C. This crude DNA extract was then used as template for
855 PCR.

856 Analysis of prime editing efficiency: The ARHGEF12 rs11824032 SNV locus (Forward
857 Primer: 5'-GTGGAGGTGGATGCCCAAC-3', Reverse Primer: 5'-
858 AATTGGGCCGACTGGGATTA-3') was amplified using primers. The subsequent
859 amplicon was processed by Genewiz for their Sanger sequencing service. Editing
860 efficiency analysis was performed using EditCo's ICE Analysis tool (ICE CRISPR
861 Analysis. 2025. v3.0. EditCo Bio: https://ice.editco.bio/#/).

862 **Statistical analysis**

863 For the quantitative gene and protein expression data, as well as *ΔF/F0*, all data are
864 represented as mean ± SEM. Each experiment was conducted in triplicate for statistical
865 analysis. Differences in gene transcript and protein expression, *ΔF/F0* between control
866 and POAG hiPSC-RGCs and hTMCs were analyzed using the Student's *t* test for two-

867 group comparison by statistical software (GraphPad Prism 10.0; GraphPad Software,
868 Inc., La Jolla, CA, USA). *p-values of < 0.05 were considered statistically significant.
869

870 **References**

871 1. Klein RJ, Zeiss C, Chew EY, et al. Complement factor H polymorphism in age-related
872 macular degeneration. *Science*. 2005;308(5720):385–389. doi:
873 10.1126/science.1109557.

874 2. Yengo L, Vedantam S, Marouli E, et al. A saturated map of common genetic variants
875 associated with human height. *Nature*. 2022;610(7933):704–712. doi: 10.1038/s41586-
876 022-05275-y.

877 3. Schizophrenia Working Group of the Psychiatric Genomics Consortium. Biological
878 insights from 108 schizophrenia-associated genetic loci. *Nature*. 2014;511(7510):421–
879 427. doi: 10.1038/nature13595.

880 4. Maurano MT, Humbert R, Rynes E, et al. Systematic localization of common disease-
881 associated variation in regulatory DNA. *Science*. 2012;337(6099):1190–1195. doi:
882 10.1126/science.1222794.

883 5. Gallagher MD, Chen-Plotkin AS. The post-GWAS era: From association to function.
884 *Am J Hum Genet*. 2018;102(5):717–730. doi: 10.1016/j.ajhg.2018.04.002.

885 6. Chesi A, Wagley Y, Johnson ME, et al. Genome-scale capture C promoter
886 interactions implicate effector genes at GWAS loci for bone mineral density. *Nature*

887 *Communications*. 2019;10(1):1260. https://doi.org/10.1038/s41467-019-09302-x. doi:
888 10.1038/s41467-019-09302-x.

889 7. Schaub MA, Boyle AP, Kundaje A, Batzoglou S, Snyder M. Linking disease
890 associations with regulatory information in the human genome. *Genome Res*.
891 2012;22(9):1748–1759. doi: 10.1101/gr.136127.111.

892 8. Pahl MC, Liu L, Pippin JA, et al. Variant to gene mapping for carpal tunnel syndrome
893 risk loci implicates skeletal muscle regulatory elements. *eBioMedicine*.
894 2024;101:105038.
895 https://www.sciencedirect.com/science/article/pii/S2352396424000732. doi:
896 10.1016/j.ebiom.2024.105038.

897 9. Ratnapriya R, Sosina OA, Starostik MR, et al. Retinal transcriptome and eQTL
898 analyses identify genes associated with age-related macular degeneration. *Nat Genet*.
899 2019;51(4):606–610. doi: 10.1038/s41588-019-0351-9.

900 10. Marchal C, Singh N, Batz Z, et al. High-resolution genome topology of human retina
901 uncovers super enhancer-promoter interactions at tissue-specific and multifactorial
902 disease loci. *Nature Communications*. 2022;13(1):5827. https://doi.org/10.1038/s41467-
903 022-33427-1. doi: 10.1038/s41467-022-33427-1.

904 11. Orozco LD, Chen H, Cox C, et al. Integration of eQTL and a single-cell atlas in the
905 human eye identifies causal genes for age-related macular degeneration. *Cell Rep*.
906 2020;30(4):1246–1259.e6. doi: 10.1016/j.celrep.2019.12.082.

907 12. Wang SK, Nair S, Li R, et al. Single-cell multiome of the human retina and deep
908 learning nominate causal variants in complex eye diseases. *Cell Genom*.
909 2022;2(8):100164. doi: 10.1016/j.xgen.2022.100164. Epub 2022 Jul 27. doi:
910 10.1016/j.xgen.2022.100164.

911 13. Javierre BM, Burren OS, Wilder SP, et al. Lineage-specific genome architecture
912 links enhancers and non-coding disease variants to target gene promoters. *Cell*.
913 2016;167(5):1369–1384.e19. doi: 10.1016/j.cell.2016.09.037.

914 14. Downes DJ, Cross AR, Hua P, et al. Identification of LZTFL1 as a candidate effector
915 gene at a COVID-19 risk locus. *Nat Genet*. 2021;53(11):1606–1615. doi:
916 10.1038/s41588-021-00955-3.

917 15. Schnitzler GR, Kang H, Fang S, et al. Convergence of coronary artery disease
918 genes onto endothelial cell programs. *Nature*. 2024;626(8000):799–807. doi:
919 10.1038/s41586-024-07022-x.

920 16. Jerkovic I, Cavalli G. Understanding 3D genome organization by multidisciplinary
921 methods. *Nat Rev Mol Cell Biol*. 2021;22(8):511–528. doi: 10.1038/s41580-021-00362-
922 w.

923 17. Bonev B, Cavalli G. Organization and function of the 3D genome. *Nature Reviews*
924 *Genetics*. 2016;17(11):661–678. https://doi.org/10.1038/nrg.2016.112. doi:
925 10.1038/nrg.2016.112.

926 18. Palmer ND, Hester JM, An SS, et al. Resequencing and analysis of variation in the
927 TCF7L2 gene in african americans suggests that SNP rs7903146 is the causal diabetes
928 susceptibility variant. *Diabetes*. 2011;60(2):662–668. doi: 10.2337/db10-0134.

929 19. Grant SFA, Thorleifsson G, Reynisdottir I, et al. Variant of transcription factor 7-like
930 2 (TCF7L2) gene confers risk of type 2 diabetes. *Nat Genet*. 2006;38(3):320–323. doi:
931 10.1038/ng1732.

932 20. Xia Q, Chesi A, Manduchi E, et al. The type 2 diabetes presumed causal variant
933 within TCF7L2 resides in an element that controls the expression of ACSL5.
934 *Diabetologia*. 2016;59(11):2360–2368. doi: 10.1007/s00125-016-4077-2.

935 21. Smemo S, Tena JJ, Kim K, et al. Obesity-associated variants within FTO form long-
936 range functional connections with IRX3. *Nature*. 2014;507(7492):371–375.
937 https://doi.org/10.1038/nature13138. doi: 10.1038/nature13138.

938 22. Claussnitzer M, Dankel SN, Kim K, et al. FTO obesity variant circuitry and adipocyte
939 browning in humans. *N Engl J Med*. 2015;373(10):895–907. doi:
940 10.1056/NEJMoa1502214.

941 23. Rosen CJ, Ingelfinger JR. Unraveling the function of FTO variants. *N Engl J Med*.
942 2015;373(10):964–965. doi: 10.1056/NEJMe1508683.

943 24. Su C, Gao L, May CL, et al. 3D chromatin maps of the human pancreas reveal
944 lineage-specific regulatory architecture of T2D risk. *Cell Metab*. 2022;34(9):1394–
945 1409.e4. doi: 10.1016/j.cmet.2022.08.014.

946 25. Yang J, McGovern A, Martin P, et al. Analysis of chromatin organization and gene
947 expression in T cells identifies functional genes for rheumatoid arthritis. *Nature*
948 *Communications*. 2020;11(1):4402. https://doi.org/10.1038/s41467-020-18180-7. doi:
949 10.1038/s41467-020-18180-7.

950 26. Quigley HA, Broman AT. The number of people with glaucoma worldwide in 2010
951 and 2020. *Br J Ophthalmol*. 2006;90(3):262–267.

952 27. Tielsch JM, Katz J, Sommer A, Quigley HA, Javitt JC. Family history and risk of
953 primary open angle glaucoma. the baltimore eye survey. *Arch Ophthalmol*.
954 1994;112(1):69–73. doi: 10.1001/archopht.1994.01090130079022 [doi].

955 28. Muñoz B, West SK, Rubin GS, et al. Causes of blindness and visual impairment in a
956 population of older americans: The salisbury eye evaluation study. *Arch Ophthalmol*.
957 2000;118(6):819–825. doi: 10.1001/archopht.118.6.819.

958 29. Cuellar-Partida G, Craig JE, Burdon KP, et al. Assessment of polygenic effects links
959 primary open-angle glaucoma and age-related macular degeneration. *Sci Rep*.
960 2016;6:26885. doi: 10.1038/srep26885.

961 30. Teikari JM. Genetic factors in open-angle (simple and capsular) glaucoma. A
962 population-based twin study. *Acta Ophthalmol (Copenh)*. 1987;65(6):715–720. doi:
963 10.1111/j.1755-3768.1987.tb07069.x.

964 31. Sanfilippo PG, Hewitt AW, Hammond CJ, Mackey DA. The heritability of ocular
965 traits. *Surv Ophthalmol*. 2010;55(6):561–583. doi: 10.1016/j.survophthal.2010.07.003.

966 32. van Koolwijk LME, Despriet DDG, van Duijn CM, et al. Genetic contributions to
967 glaucoma: Heritability of intraocular pressure, retinal nerve fiber layer thickness, and
968 optic disc morphology. *Invest Ophthalmol Vis Sci*. 2007;48(8):3669–3676. doi:
969 10.1167/iovs.06-1519.

970 33. Awadalla MS, Fingert JH, Roos BE, et al. Copy number variations of TBK1 in
971 australian patients with primary open-angle glaucoma. *Am J Ophthalmol*.
972 2015;159(1):124–30.e1. doi: 10.1016/j.ajo.2014.09.044.

973 34. Rezaie R, Child C, Hitchings H, et al. Adult-onset primary open-angle glaucoma
974 caused by mutations in optineurin. *Science*. 2002;295(5557):1077–1079.
975 https://doi.org/10.1126/science.1066901. doi: 10.1126/science.1066901.

976 35. Stone EM, Fingert JH, Alward WL, et al. Identification of a gene that causes primary
977 open angle glaucoma. *Science*. 1997;275(5300):668–670. doi:
978 10.1126/science.275.5300.668.

979 36. Sakurada Y, Mabuchi F, Kashiwagi K. Genetics of primary open-angle glaucoma
980 and its endophenotypes. *Prog Brain Res*. 2020;256(1):31–47. doi:
981 10.1016/bs.pbr.2020.06.001.

982 37. Verma SS, Gudiseva HV, Chavali VRM, et al. A multi-cohort genome-wide
983 association study in african ancestry individuals reveals risk loci for primary open-angle
984 glaucoma. *Cell*. 2024;187(2):464–480.e10.
985 https://www.sciencedirect.com/science/article/pii/S0092867423013387. doi:
986 10.1016/j.cell.2023.12.006.

987 38. Singh N, Kizhatil K, Duraikannu D, Choquet H, Saidas Nair K. Structural framework
988 to address variant-gene relationship in primary open-angle glaucoma. *Vision Res*.
989 2025;226:108505.
990 https://www.sciencedirect.com/science/article/pii/S0042698924001494. doi:
991 10.1016/j.visres.2024.108505.

992 39. Choquet H, Wiggs JL, Khawaja AP. Clinical implications of recent advances in
993 primary open-angle glaucoma genetics. *Eye (Lond)*. 2020;34(1):29–39. doi:
994 10.1038/s41433-019-0632-7.

995 40. Choquet H, Paylakhi S, Kneeland SC, et al. A multiethnic genome-wide association
996 study of primary open-angle glaucoma identifies novel risk loci. *Nat Commun*.
997 2018;9(1):2278–4. doi: 10.1038/s41467-018-04555-4.

998 41. Springelkamp H, Iglesias AI, Cuellar-Partida G, et al. ARHGEF12 influences the risk
999 of glaucoma by increasing intraocular pressure. *Hum Mol Genet*. 2015;24(9):2689–
1000 2699. doi: 10.1093/hmg/ddv027.

1001 42. Wiggs JL, Yaspan BL, Hauser MA, et al. Common variants at 9p21 and 8q22 are
1002 associated with increased susceptibility to optic nerve degeneration in glaucoma. *PLoS*
1003 *Genet*. 2012;8(4):e1002654. doi: 10.1371/journal.pgen.1002654.

1004 43. Thorleifsson G, Walters GB, Hewitt AW, et al. Common variants near CAV1 and
1005 CAV2 are associated with primary open-angle glaucoma. *Nat Genet*. 2010;42(10):906–
1006 909. doi: 10.1038/ng.661.

1007 44. Han X, Gharahkhani P, Hamel AR, et al. Large-scale multitrait genome-wide
1008 association analyses identify hundreds of glaucoma risk loci. *Nat Genet*.
1009 2023;55(7):1116–1125. https://doi.org/10.1038/s41588-023-01428-5. doi:
1010 10.1038/s41588-023-01428-5.

1011 45. Gharahkhani P, Jorgenson E, Hysi P, et al. Genome-wide meta-analysis identifies
1012 127 open-angle glaucoma loci with consistent effect across ancestries. *Nat Commun*.
1013 2021;12(1):1258–4. doi: 10.1038/s41467-020-20851-4.

1014 46. Bailey JNC, Loomis SJ, Kang JH, et al. Genome-wide association analysis identifies
1015 TXNRD2, ATXN2 and FOXC1 as susceptibility loci for primary open-angle glaucoma.
1016 *Nat Genet*. 2016;48(2):189–194. doi: 10.1038/ng.3482.

1017 47. Gharahkhani P, Burdon KP, Fogarty R, et al. Common variants near ABCA1,
1018 AFAP1 and GMDS confer risk of primary open-angle glaucoma. *Nat Genet*.
1019 2014;46(10):1120–1125. doi: 10.1038/ng.3079.

1020 48. Burdon KP. Genome-wide association studies in the hunt for genes causing primary
1021 open-angle glaucoma: A review. *Clin Exp Ophthalmol*. 2012;40(4):358–363. doi:
1022 10.1111/j.1442-9071.2011.02744.x.

1023 49. Shiga Y, Akiyama M, Nishiguchi KM, et al. Genome-wide association study
1024 identifies seven novel susceptibility loci for primary open-angle glaucoma. *Hum Mol*
1025 *Genet*. 2018;27(8):1486–1496. doi: 10.1093/hmg/ddy053.

1026 50. Lo Faro V, Bhattacharya A, Zhou W, et al. Novel ancestry-specific primary open-
1027 angle glaucoma loci and shared biology with vascular mechanisms and cell
1028 proliferation. *Cell Rep Med*. 2024;5(2):101430. doi: 10.1016/j.xcrm.2024.101430.

1029 51. MacGregor S, Ong J, An J, et al. Genome-wide association study of intraocular
1030 pressure uncovers new pathways to glaucoma. *Nat Genet*. 2018;50(8):1067–1071. doi:
1031 10.1038/s41588-018-0176-y.

1032 52. Osman W, Low S, Takahashi A, Kubo M, Nakamura Y. A genome-wide association
1033 study in the japanese population confirms 9p21 and 14q23 as susceptibility loci for
1034 primary open angle glaucoma. *Hum Mol Genet*. 2012;21(12):2836–2842. doi:
1035 10.1093/hmg/dds103.

1036 53. Chen Y, Lin Y, Vithana EN, et al. Common variants near ABCA1 and in PMM2 are
1037 associated with primary open-angle glaucoma. *Nat Genet*. 2014;46(10):1115–1119.
1038 https://doi.org/10.1038/ng.3078. doi: 10.1038/ng.3078.

1039 54. Trang KB, Sharma P, Cook L, et al. 3D chromatin-based variant-to-gene maps
1040 across 57 human cell types reveal the cellular and genetic architecture of autoimmune
1041 disease susceptibility. *Genome Biol*. 2025;26(1):414–4. doi: 10.1186/s13059-025-
1042 03880-4.

1043 55. Palermo P, Chesi C, Zimmerman Z, et al. Variant-to-gene mapping followed by
1044 cross-species genetic screening identifies GPI-anchor biosynthesis as a regulator of
1045 sleep. *Sci Adv*. 2023;9(1):eabq0844. https://doi.org/10.1126/sciadv.abq0844. doi:
1046 10.1126/sciadv.abq0844.

1047 56. Thulson E, Davis ES, D'Costa S, et al. 3D chromatin structure in chondrocytes
1048 identifies putative osteoarthritis risk genes. *Genetics*. 2022;222(4):iyac141. doi:
1049 10.1093/genetics/iyac141. doi: 10.1093/genetics/iyac141.

1050 57. Cairns J, Freire-Pritchett P, Wingett SW, et al. CHiCAGO: Robust detection of DNA
1051 looping interactions in capture hi-C data. *Genome Biol*. 2016;17(1):127–2. doi:
1052 10.1186/s13059-016-0992-2.

1053 58. Roayaei Ardakany A, Gezer HT, Lonardi S, Ay F. Mustache: Multi-scale detection of
1054 chromatin loops from hi-C and micro-C maps using scale-space representation.
1055 *Genome Biol*. 2020;21(1):256–0. doi: 10.1186/s13059-020-02167-0.

1056 59. Kaul A, Bhattacharyya S, Ay F. Identifying statistically significant chromatin contacts
1057 from hi-C data with FitHiC2. *Nat Protoc*. 2020;15(3):991–1012. doi: 10.1038/s41596-
1058 019-0273-0.

1059 60. Steely HT, Browder SL, Julian MB, Miggans ST, Wilson KL, Clark AF. The effects of
1060 dexamethasone on fibronectin expression in cultured human trabecular meshwork cells.
1061 *Invest Ophthalmol Vis Sci*. 1992;33(7):2242–2250.

1062 61. Schmelter C, Fomo KN, Brueck A, et al. Glaucoma-associated CDR1 peptide
1063 promotes RGC survival in retinal explants through molecular interaction with acidic
1064 leucine rich nuclear phosphoprotein 32A (ANP32A). *Biomolecules*. 2023;13(7):1161.
1065 doi: 10.3390/biom13071161. doi: 10.3390/biom13071161.

1066 62. Verma A, Huffman JE, Rodriguez A, et al. Diversity and scale: Genetic architecture
1067 of 2068 traits in the VA million veteran program. *Science*. 2024;385(6706):eadj1182.
1068 doi: 10.1126/science.adj1182.

1069 63. Bonnemaijer PWM, Leeuwen EMv, Iglesias AI, et al. Multi-trait genome-wide
1070 association study identifies new loci associated with optic disc parameters. *Commun*
1071 *Biol*. 2019;2:435–9. eCollection 2019. doi: 10.1038/s42003-019-0634-9.

1072 64. Carey CE, Shafee R, Wedow R, et al. Principled distillation of UK biobank
1073 phenotype data reveals underlying structure in human variation. *Nat Hum Behav*.
1074 2024;8(8):1599–1615. doi: 10.1038/s41562-024-01909-5.

1075 65. Scerri TS, Quaglieri A, Cai C, et al. Genome-wide analyses identify common
1076 variants associated with macular telangiectasia type 2. *Nat Genet*. 2017;49(4):559–567.
1077 doi: 10.1038/ng.3799.

1078 66. Zakharia F, Basu A, Absher D, et al. Characterizing the admixed african ancestry of
1079 african americans. *Genome Biol*. 2009;10(12):R141–r141. Epub 2009 Dec 22. doi:
1080 10.1186/gb-2009-10-12-r141.

1081 67. Luo Y, Li X, Wang X, et al. Estimating heritability and its enrichment in tissue-
1082 specific gene sets in admixed populations. *Hum Mol Genet*. 2021;30(16):1521–1534.
1083 doi: 10.1093/hmg/ddab130.

1084 68. Huang L, Rosen JD, Sun Q, et al. TOP-LD: A tool to explore linkage disequilibrium
1085 with TOPMed whole-genome sequence data. *Am J Hum Genet*. 2022;109(6):1175–
1086 1181. doi: 10.1016/j.ajhg.2022.04.006.

1087 69. Machiela MJ, Chanock SJ. LDlink: A web-based application for exploring
1088 population-specific haplotype structure and linking correlated alleles of possible
1089 functional variants. *Bioinformatics*. 2015;31(21):3555–3557. doi:
1090 10.1093/bioinformatics/btv402.

1091 70. Keller KE, Bhattacharya SK, Borrás T, et al. Consensus recommendations for
1092 trabecular meshwork cell isolation, characterization and culture. *Exp Eye Res*.
1093 2018;171:164–173. doi: 10.1016/j.exer.2018.03.001.

1094 71. Vrathasha V, Nikonov S, Bell BA, et al. Transplanted human iPSC-derived retinal
1095 ganglion cells integrate into mouse retinas and are electrophysiologically functional.
1096 *iScience*. 2022:105308.
1097 https://www.sciencedirect.com/science/article/pii/S2589004222015802. doi:
1098 https://doi.org/10.1016/j.isci.2022.105308.

1099 72. Gudiseva HV, Vrathasha V, He J, Bungatavula D, O'Brien JM, Chavali VRM. Single
1100 cell sequencing of induced pluripotent stem cell derived retinal ganglion cells (iPSC-
1101 RGC) reveals distinct molecular signatures and RGC subtypes. *Genes*. 2021;12(12).
1102 doi: 10.3390/genes12122015.

1103 73. Chavali VRM, Haider N, Rathi S, et al. Dual SMAD inhibition and wnt inhibition
1104 enable efficient and reproducible differentiations of induced pluripotent stem cells into

1105 retinal ganglion cells. *Scientific Reports*. 2020;10(1):11828.
1106 https://doi.org/10.1038/s41598-020-68811-8. doi: 10.1038/s41598-020-68811-8.

1107 74. Capetian P, Müller L, Volkmann J, Heckmann M, Ergün S, Wagner N. Visualizing
1108 the synaptic and cellular ultrastructure in neurons differentiated from human induced
1109 neural stem cells-an optimized protocol. *Int J Mol Sci*. 2020;21(5):1708. doi:
1110 10.3390/ijms21051708. doi: 10.3390/ijms21051708.

1111 75. Tian L, Hires SA, Mao T, et al. Imaging neural activity in worms, flies and mice with
1112 improved GCaMP calcium indicators. *Nat Methods*. 2009;6(12):875–881. doi:
1113 10.1038/nmeth.1398.

1114 76. Rumyantsev OI, Lecoq JA, Hernandez O, et al. Fundamental bounds on the fidelity
1115 of sensory cortical coding. *Nature*. 2020;580(7801):100–105.
1116 https://doi.org/10.1038/s41586-020-2130-2. doi: 10.1038/s41586-020-2130-2.

1117 77. Chen Q, Cichon J, Wang W, et al. Imaging neural activity using Thy1-GCaMP
1118 transgenic mice. *Neuron*. 2012;76(2):297–308. doi: 10.1016/j.neuron.2012.07.011.

1119 78. Kwon YH, Fingert JH, Kuehn MH, Alward WLM. Primary open-angle glaucoma. *N*
1120 *Engl J Med*. 2009;360(11):1113–1124. doi: 10.1056/NEJMra0804630.

1121 79. Aptel F, Aryal-Charles N, Giraud J, et al. Progression of visual field in patients with
1122 primary open-angle glaucoma - ProgF study 1. *Acta Ophthalmol*. 2015;93(8):615. doi:
1123 10.1111/aos.12788.

1124 80. Heijl A, Leske MC, Bengtsson B, et al. Reduction of intraocular pressure and
1125 glaucoma progression: Results from the early manifest glaucoma trial. *Arch Ophthalmol*.
1126 2002;120(10):1268–1279. doi: 10.1001/archopht.120.10.1268.

1127 81. Weinreb RN, Aung T, Medeiros FA. The pathophysiology and treatment of
1128 glaucoma: A review. *JAMA*. 2014;311(18):1901–1911.

1129 82. Yuan Y, Biswas P, Zemke NR, et al. Single-cell analysis of the epigenome and 3D
1130 chromatin architecture in the human retina. *bioRxiv*. 2025. doi:
1131 10.1101/2024.12.28.630634.

1132 83. Gao XR, Huang H, Nannini DR, Fan F, Kim H. Genome-wide association analyses
1133 identify new loci influencing intraocular pressure. *Hum Mol Genet*. 2018;27(12):2205–
1134 2213. doi: 10.1093/hmg/ddy111.

1135 84. Springelkamp H, Iglesias AI, Mishra A, et al. New insights into the genetics of
1136 primary open-angle glaucoma based on meta-analyses of intraocular pressure and optic
1137 disc characteristics. *Hum Mol Genet*. 2017;26(2):438–453. doi: 10.1093/hmg/ddw399.

1138 85. Wistow G, Peterson K, Gao J, et al. NEIBank: Genomics and bioinformatics
1139 resources for vision research. *Mol Vis*. 2008;14:1327–1337.

1140 86. Macosko EZ, Basu A, Satija R, et al. Highly parallel genome-wide expression
1141 profiling of individual cells using nanoliter droplets. *Cell*. 2015;161(5):1202–1214.
1142 https://doi.org/10.1016/j.cell.2015.05.002. doi: 10.1016/j.cell.2015.05.002.

1143 87. Wang J, Liu X, Zhong Y. Rho/rho-associated kinase pathway in glaucoma (review).
1144 *Int J Oncol*. 2013;43(5):1357–1367. doi: 10.3892/ijo.2013.2100.

1145 88. Fukuhara S, Chikumi H, Gutkind JS. Leukemia-associated rho guanine nucleotide
1146 exchange factor (LARG) links heterotrimeric G proteins of the G(12) family to rho. *FEBS*
1147 *Lett*. 2000;485(2-3):183–188. doi: 10.1016/s0014-5793(00)02224-9.

1148 89. Pattabiraman PP, Maddala R, Rao PV. Regulation of plasticity and fibrogenic
1149 activity of trabecular meshwork cells by rho GTPase signaling. *J Cell Physiol*.
1150 2014;229(7):927–942. https://pubmed.ncbi.nlm.nih.gov/24318513
1151 https://www.ncbi.nlm.nih.gov/pmc/articles/PMC3965649/. doi: 10.1002/jcp.24524.

1152 90. Li L, Feng X, Fang F, et al. Longitudinal in vivo Ca2+ imaging reveals dynamic
1153 activity changes of diseased retinal ganglion cells at the single-cell level. *Proceedings of*
1154 *the National Academy of Sciences*. 2022;119(48):e2206829119.
1155 https://doi.org/10.1073/pnas.2206829119. doi: 10.1073/pnas.2206829119.

1156 91. Wienbar S, Schwartz GW. The dynamic receptive fields of retinal ganglion cells.
1157 *Prog Retin Eye Res*. 2018;67:102–117. doi: 10.1016/j.preteyeres.2018.06.003.

1158 92. Sanes JR, Masland RH. The types of retinal ganglion cells: Current status and
1159 implications for neuronal classification. *Annu Rev Neurosci*. 2015;38:221–246. doi:
1160 10.1146/annurev-neuro-071714-034120.

1161 93. Chichilnisky EJ, Kalmar RS. Functional asymmetries in ON and OFF ganglion cells
1162 of primate retina. *J Neurosci*. 2002;22(7):2737–2747. doi: 10.1523/JNEUROSCI.22-07-
1163 02737.2002.

1164 94. Fiscella M, Farrow K, Jones IL, et al. Recording from defined populations of retinal
1165 ganglion cells using a high-density CMOS-integrated microelectrode array with real-time
1166 switchable electrode selection. *J Neurosci Methods*. 2012;211(1):103–113. doi:
1167 10.1016/j.jneumeth.2012.08.017.

1168 95. Wang M, Zheng Y. Oxidative stress and antioxidants in the trabecular meshwork.
1169 *PeerJ*. 2019;7:e8121. doi: 10.7717/peerj.8121.

1170 96. Ammar DA, Hamweyah KM, Kahook MY. Antioxidants protect trabecular meshwork
1171 cells from hydrogen peroxide-induced cell death. *Translational Vision Science &*
1172 *Technology*. 2012;1(1):4.

1173 97. Böhm EW, Buonfiglio F, Voigt AM, et al. Oxidative stress in the eye and its role in
1174 the pathophysiology of ocular diseases. *Redox Biology*. 2023;68:102967.
1175 https://www.sciencedirect.com/science/article/pii/S2213231723003683. doi:
1176 10.1016/j.redox.2023.102967.

1177 98. Majsterek I, Malinowska K, Stanczyk M, et al. Evaluation of oxidative stress markers
1178 in pathogenesis of primary open-angle glaucoma. *Exp Mol Pathol*. 2011;90(2):231–237.

1179 99. Reis LM, Seese S, Maheshwari M, et al. Novel genetic diagnoses in septo-optic
1180 dysplasia. *Genes (Basel)*. 2022;13(7):1165. doi: 10.3390/genes13071165. doi:
1181 10.3390/genes13071165.

1182 100. Wu JI, Rajendra R, Barsi JC, et al. Targeted disruption of Mib2 causes
1183 exencephaly with a variable penetrance. *Genesis*. 2007;45(11):722–727.

1184 101. Jaglin XH, Poirier K, Saillour Y, et al. Mutations in the beta-tubulin gene TUBB2B
1185 result in asymmetrical polymicrogyria. *Nat Genet*. 2009;41(6):746–752. doi:
1186 10.1038/ng.380.

1187 102. Cederquist GY, Luchniak A, Tischfield MA, et al. An inherited TUBB2B mutation
1188 alters a kinesin-binding site and causes polymicrogyria, CFEOM and axon
1189 dysinnervation. *Hum Mol Genet*. 2012;21(26):5484–5499. doi: 10.1093/hmg/dds393.

1190 103. Ugalde-Triviño L, Tejeda GS, Esteban-Ortega GM, Díaz-Guerra M. A brain-
1191 accessible peptide modulates stroke inflammatory response and neurotoxicity by
1192 targeting BDNF-receptor TrkB-T1 specific interactome. *Theranostics*.
1193 2025;15(10):4654–4672. doi: 10.7150/thno.111272.

1194 104. Zhang M, Deng Y, Luo Y, et al. Control of BACE1 degradation and APP
1195 processing by ubiquitin carboxyl-terminal hydrolase L1. *J Neurochem*.
1196 2012;120(6):1129–1138. doi: 10.1111/j.1471-4159.2011.07644.x.

1197 105. Bilguvar K, Tyagi NK, Ozkara C, et al. Recessive loss of function of the neuronal
1198 ubiquitin hydrolase UCHL1 leads to early-onset progressive neurodegeneration. *Proc*
1199 *Natl Acad Sci U S A*. 2013;110(9):3489–3494. doi: 10.1073/pnas.1222732110.

1200 106. Mehalow AK, Kameya S, Smith RS, et al. CRB1 is essential for external limiting
1201 membrane integrity and photoreceptor morphogenesis in the mammalian retina. *Hum*
1202 *Mol Genet*. 2003;12(17):2179–2189. doi: 10.1093/hmg/ddg232.

1203 107. Weleber RG. Infantile and childhood retinal blindness: A molecular perspective
1204 (the franceschetti lecture). *Ophthalmic Genet*. 2002;23(2):71–97. doi:
1205 10.1076/opge.23.2.71.2214.

1206 108. Massey-Harroche D, Delgrossi M, Lane-Guermonprez L, et al. Evidence for a
1207 molecular link between the tuberous sclerosis complex and the crumbs complex. *Hum*
1208 *Mol Genet*. 2007;16(5):529–536. doi: 10.1093/hmg/ddl485.

1209 109. Kukekova AV, Nelson J, Kuchtey RW, et al. Linkage mapping of canine rod cone
1210 dysplasia type 2 (rcd2) to CFA7, the canine orthologue of human 1q32. *Invest*
1211 *Ophthalmol Vis Sci*. 2006;47(3):1210–1215. doi: 10.1167/iovs.05-0861.

1212 110. van de Pavert SA, Meuleman J, Malysheva A, et al. A single amino acid
1213 substitution (Cys249Trp) in Crb1 causes retinal degeneration and deregulates
1214 expression of pituitary tumor transforming gene Pttg1. *J Neurosci*. 2007;27(3):564–573.
1215 doi: 10.1523/JNEUROSCI.3496-06.2007.

1216 111. Stehle IF, Imventarza JA, Woerz F, et al. Human CRB1 and CRB2 form homo- and
1217 heteromeric protein complexes in the retina. *Life Sci Alliance*. 2024;7(6):e202302440.
1218 doi: 10.26508/lsa.202302440. Print 2024 Jun. doi: 10.26508/lsa.202302440.

1219 112. Sylla MM, Kolesinkova M, da Costa BL, Maumenee IH, Tsang SH, Quinn PMJ. A
1220 novel pathogenic CRB1 variant presenting as leber congenital amaurosis 8 and
1221 evaluation of gene editing feasibility. *Doc Ophthalmol*. 2023;147(3):217–224. doi:
1222 10.1007/s10633-023-09951-w.

1223 113. Lopes da Costa B, Kolesnikova M, Levi SR, et al. Clinical and therapeutic
1224 evaluation of the ten most prevalent CRB1 mutations. *Biomedicines*. 2023;11(2):385.
1225 doi: 10.3390/biomedicines11020385. doi: 10.3390/biomedicines11020385.

1226 114. Di Donato N, Neuhann T, Kahlert A, et al. Mutations in EXOSC2 are associated
1227 with a novel syndrome characterised by retinitis pigmentosa, progressive hearing loss,
1228 premature ageing, short stature, mild intellectual disability and distinctive gestalt. *J Med*
1229 *Genet*. 2016;53(6):419–425. doi: 10.1136/jmedgenet-2015-103511.

1230 115. Weatherly SM, Collin GB, Charette JR, et al. Identification of Arhgef12 and prkci as
1231 genetic modifiers of retinal dysplasia in the Crb1rd8 mouse model. *PLoS Genet*.
1232 2022;18(6):e1009798. doi: 10.1371/journal.pgen.1009798.

1233 116. Manavathi B, Peng S, Rayala SK, et al. Repression of Six3 by a corepressor
1234 regulates rhodopsin expression. *Proc Natl Acad Sci U S A*. 2007;104(32):13128–13133.
1235 doi: 10.1073/pnas.0705878104.

1236 117. Bock C, Datlinger P, Chardon F, et al. High-content CRISPR screening. *Nature*
1237 *Reviews Methods Primers*. 2022;2(1):8. https://doi.org/10.1038/s43586-021-00093-4.
1238 doi: 10.1038/s43586-021-00093-4.

1239 118. Duong TT, Vasireddy V, Ramachandran P, et al. Use of induced pluripotent stem
1240 cell models to probe the pathogenesis of choroideremia and to develop a potential
1241 treatment. *Stem cell research*. 2018;27:140–150.

1242 119. Sullivan SK, Mills JA, Koukouritaki SB, et al. High-level transgene expression in
1243 induced pluripotent stem cell–derived megakaryocytes: Correction of glanzmann
1244 thrombasthenia. *Blood*. 2014;123(5):753–757.

1245 120. Maguire JA, Gagne A, Mills JA, Gadue P, French DL. Generation of human control
1246 iPS cell line CHOPWT9 from healthy adult peripheral blood mononuclear cells. *Stem*
1247 *Cell Research*. 2016;16(1):14–16.

1248 121. Espuny-Camacho I, Michelsen KA, Gall D, et al. Pyramidal neurons derived from
1249 human pluripotent stem cells integrate efficiently into mouse brain circuits in vivo.
1250 *Neuron*. 2013;77(3):440–456.

1251 122. Langmead B, Trapnell C, Pop M, Salzberg SL. Ultrafast and memory-efficient
1252 alignment of short DNA sequences to the human genome. *Genome Biol*.
1253 2009;10(3):R25–r25. Epub 2009 Mar 4. doi: 10.1186/gb-2009-10-3-r25.

1254 123. Zhang Y, Liu T, Meyer CA, et al. Model-based analysis of ChIP-seq (MACS).
1255 *Genome Biol*. 2008;9(9):R137–r137. Epub 2008 Sep 17. doi: 10.1186/gb-2008-9-9-
1256 r137.

1257 124. Ou J, Liu H, Yu J, et al. ATACseqQC: A bioconductor package for post-alignment
1258 quality assessment of ATAC-seq data. *BMC Genomics*. 2018;19(1):169–3. doi:
1259 10.1186/s12864-018-4559-3.

1260 125. Wingett S, Ewels P, Furlan-Magaril M, et al. HiCUP: Pipeline for mapping and
1261 processing hi-C data. *F1000Res*. 2015;4:1310. doi: 10.12688/f1000research.7334.1.

1262 126. Putri GH, Anders S, Pyl PT, Pimanda JE, Zanini F. Analysing high-throughput
1263 sequencing data in python with HTSeq 2.0. *Bioinformatics*. 2022;38(10):2943–2945.
1264 doi: 10.1093/bioinformatics/btac166.

1265 127. Robinson MD, McCarthy DJ, Smyth GK. edgeR: A bioconductor package for
1266 differential expression analysis of digital gene expression data. *Bioinformatics*.
1267 2010;26(1):139–140. doi: 10.1093/bioinformatics/btp616.

1268 128. Su C, Argenziano M, Lu S, et al. 3D promoter architecture re-organization during
1269 iPSC-derived neuronal cell differentiation implicates target genes for
1270 neurodevelopmental disorders. *Prog Neurobiol*. 2021;201:102000. doi:
1271 10.1016/j.pneurobio.2021.102000.

1272 129. Finucane HK, Bulik-Sullivan B, Gusev A, et al. Partitioning heritability by functional
1273 annotation using genome-wide association summary statistics. *Nat Genet*.
1274 2015;47(11):1228–1235. doi: 10.1038/ng.3404.

1275 130. Bulik-Sullivan BK, Loh P, Finucane HK, et al. LD score regression distinguishes
1276 confounding from polygenicity in genome-wide association studies. *Nat Genet*.
1277 2015;47(3):291–295. doi: 10.1038/ng.3211.

1278 131. Gazal S, Finucane HK, Furlotte NA, et al. Linkage disequilibrium-dependent
1279 architecture of human complex traits shows action of negative selection. *Nat Genet*.
1280 2017;49(10):1421–1427. doi: 10.1038/ng.3954.

1281 132. Patterson N, Price AL, Reich D. Population structure and eigenanalysis. *PLoS*
1282 *Genet*. 2006;2(12):e190. doi: 10.1371/journal.pgen.0020190.

1283 133. Lawrence M, Huber W, Pagès H, et al. Software for computing and annotating
1284 genomic ranges. *PLoS Comput Biol*. 2013;9(8):e1003118. doi:
1285 10.1371/journal.pcbi.1003118.

1286 134. Coetzee SG, Coetzee GA, Hazelett DJ. motifbreakR: An R/bioconductor package
1287 for predicting variant effects at transcription factor binding sites. *Bioinformatics*.
1288 2015;31(23):3847–3849. doi: 10.1093/bioinformatics/btv470.

1289 135. Kulakovskiy IV, Vorontsov IE, Yevshin IS, et al. HOCOMOCO: Towards a
1290 complete collection of transcription factor binding models for human and mouse via

1291 large-scale ChIP-seq analysis. *Nucleic Acids Res*. 2018;46(D1):D252–D259. doi:
1292 10.1093/nar/gkx1106.

1293 136. Borghuis BG, Tian L, Xu Y, et al. Imaging light responses of targeted neuron
1294 populations in the rodent retina. *J Neurosci*. 2011;31(8):2855–2867. doi:
1295 10.1523/JNEUROSCI.6064-10.2011.

1296 137. Chen PJ, Hussmann JA, Yan J, et al. Enhanced prime editing systems by
1297 manipulating cellular determinants of editing outcomes. *Cell*. 2021;184(22):5635–
1298 5652.e29. doi: 10.1016/j.cell.2021.09.018.

1299 138. Nelson JW, Randolph PB, Shen SP, et al. Engineered pegRNAs improve prime
1300 editing efficiency. *Nat Biotechnol*. 2022;40(3):402–410. https://doi.org/10.1038/s41587-
1301 021-01039-7. doi: 10.1038/s41587-021-01039-7.

1302 139. Lopes da Costa B, Helms KM, Theodore K, et al. Prime editing for the investigation
1303 of aberrant splicing defect associated with a pathogenic PRPH2 variant. *Mol Ther*
1304 *Nucleic Acids*. 2025;36(4):102740. doi: 10.1016/j.omtn.2025.102740.

1305 140. Caruso SM, Tsai Y, da Costa BL, et al. Prime editing strategy to install the PRPH2
1306 c.828+1G>A mutation. *Adv Exp Med Biol*. 2023;1415:97–102. doi: 10.1007/978-3-031-
1307 27681-1_15.

1308

1309

Authorship Contribution Statement

Conceptualization: V.V., M.C.P., S.F.A.G., and J.M.O.; methodology: V.V., M.C.P., S.F.A.G, and J.M.O.; software: M.C.P., Y.B., Y.Z., S.S.V., S.F.A.G., and J.M.O.; validation: V.V., M.C.P., S.F.A.G., and J.M.O.; formal analysis: V.V., M.C.P., S.F.A.G., and J.M.O.; investigation: V.V., M.C.P., J.A.P., S.N., J.H., M.H., M.L., A.A.E., H.V.G., V.R.M.C., B.L., A.M.B., A.G.R., Q.N.C., E.M.E., P.S.S., V.A.; resources: S.F.A.G. and J.M.O.; data curation: V.V., M.C.P., J.H., L.M., P.M.J.Q., S.F.A.G., and J.M.O.; writing – original draft: V.V., M.C.P., and R.J.S.; writing – review & editing: all authors; visualization: V.V., M.C.P., S.F.A.G., and J.M.O.; supervision: S.F.A.G. and J.M.O.; project administration: V.V., M.C.P., S.F.A.G., and J.M.O.; funding acquisition: S.FA.G. and J.M.O.

Financial Disclosures

The authors have no financial disclosures.

Conflicts of Interest

The authors declare no conflicts of interest.

Funding/Support

This work was supported by the National Eye Institute, Bethesda, MD (1R01EY023557) and Vision Research Core (P30 EY001583) grants. Funds also came from the F.M. Kirby Foundation, Research to Prevent Blindness, UPenn Hospital Board of Women Visitors, and Paul and Evanina Bell Mackall Foundation Trust. The Ophthalmology Department at the Perelman School of Medicine and the VA Hospital in Philadelphia, PA, also provided support. The sponsors/funding organizations had no role in the design or conduct of this

research. Penn Cytomics is partially supported by the Abramson Cancer Center NCI Grant (P30 016520). SFAG is supported by the Daniel B. Burke Endowed Chair for Diabetes Research.

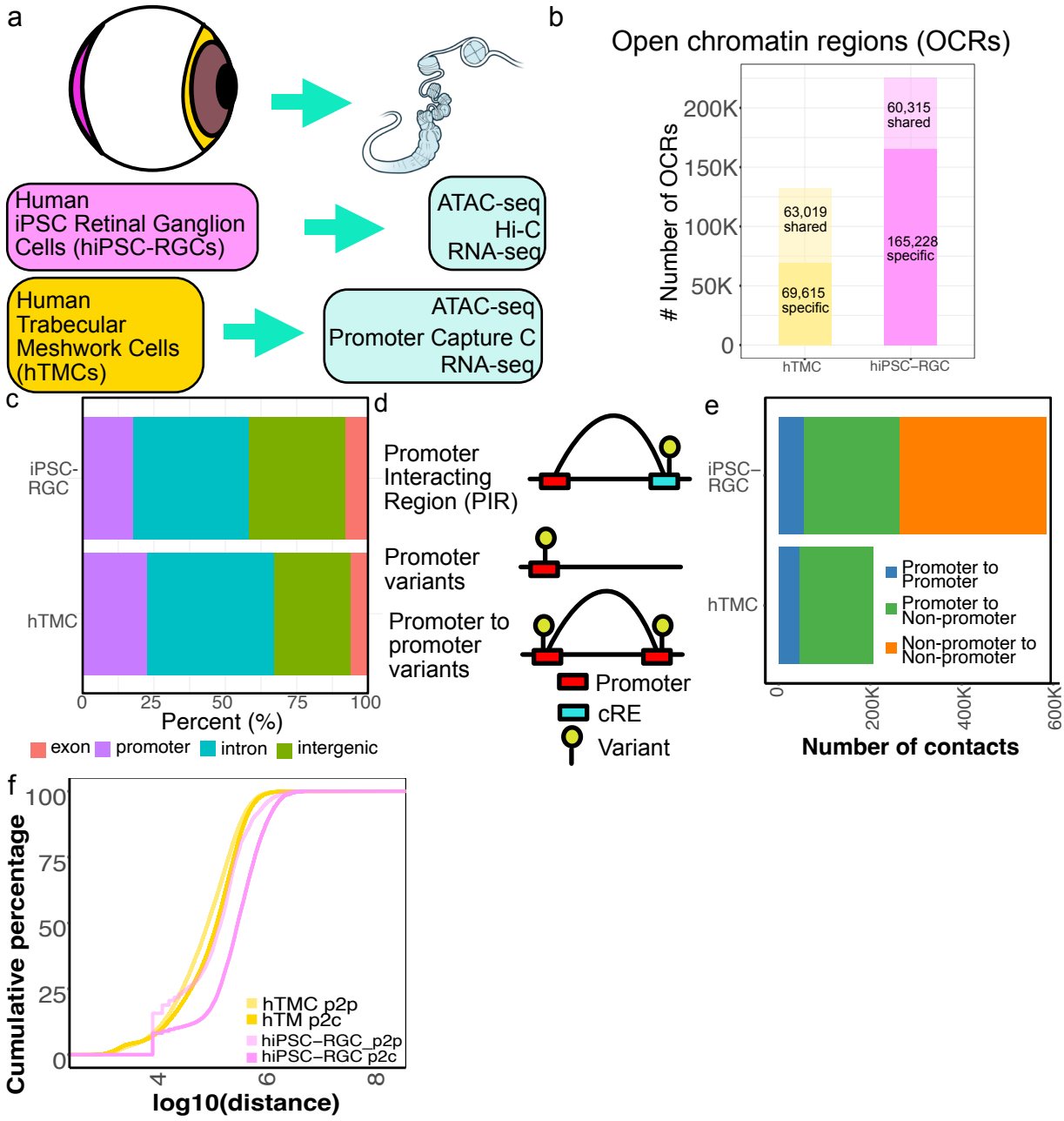

Figure 1: Constructing the cRE network of glaucoma-relevant cell types using ATAC-seq, RNA-seq, and chromatin conformation. (a) Schematic of the libraries constructed for the two cellular models of hiPSC-RGCs and hTMCs. While RNA-seq and ATAC-seq were performed on both hiPSC-RGCs and hTMC, chromatin conformation was characterized via Hi-C in hiPSC-RGCs and Promoter Focused Capture C in hTMCs. (b) The number of OCRs defined by ATAC-seq was specific to each cell type (yellow = hTMCs; pink = hiPSC-RGCs). OCRs were considered shared if there was a 1bp overlap with an OCR in the opposite cell type. (c) The proportion of OCRs falling into each category of genomic region annotations (exons, introns, intergenic, or promoter). (d) Schematic of cases for overlaying chromatin conformation with open chromatin data. Regions with significant interactions in either Promoter Focused Capture C or Hi-C are termed Promoter Interacting Regions (PIR). OCRs overlapping such regions are considered putative cREs for the targeted promoter. OCRs that overlay promoters (-1500bp/+500bp from a TSS) themselves are also considered as potential regulatory elements. Variants located in OCRs and nominated by these approaches are considered potentially regulatory. (e) The number of contacts per cell type that are between a promoter and a non-promoter region, between two promoters, or between two non-promoter regions (only found in Hi-C). (f) The cumulative distribution of the distance of significant chromatin interactions called in hTMCs and hiPSC-RGCs, stratified by either promoter to non-promoter (p2c) or promoter to promoter (p2p).

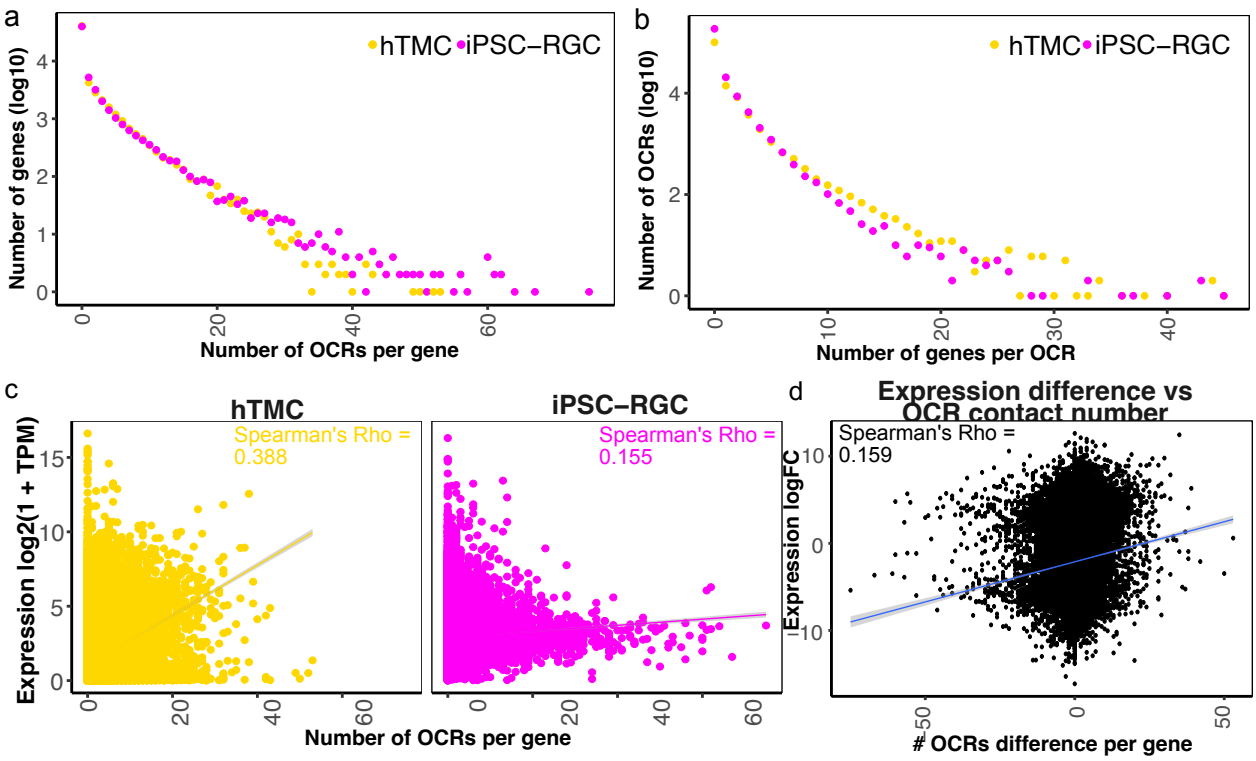

Figure 2: Promoter-connected OCRs are correlated with increased gene expression. (a) The number of OCRs per gene versus the log-scaled number of genes with the specified number of OCRs in each cell type (pink = hiPSC-RGC; yellow = hTMC). (b) The number of genes connected per log-scaled OCR for each cell type. (c) The number of OCRs contacting a gene promoter versus expression quantified in log2(1+TPM) for each cell type. d) The difference in expression against the difference in the number of OCRs predicted to be connected to each gene. In (c) and (d), the trend line from the linear association is shown with the shaded region representing 95% confidence interval.

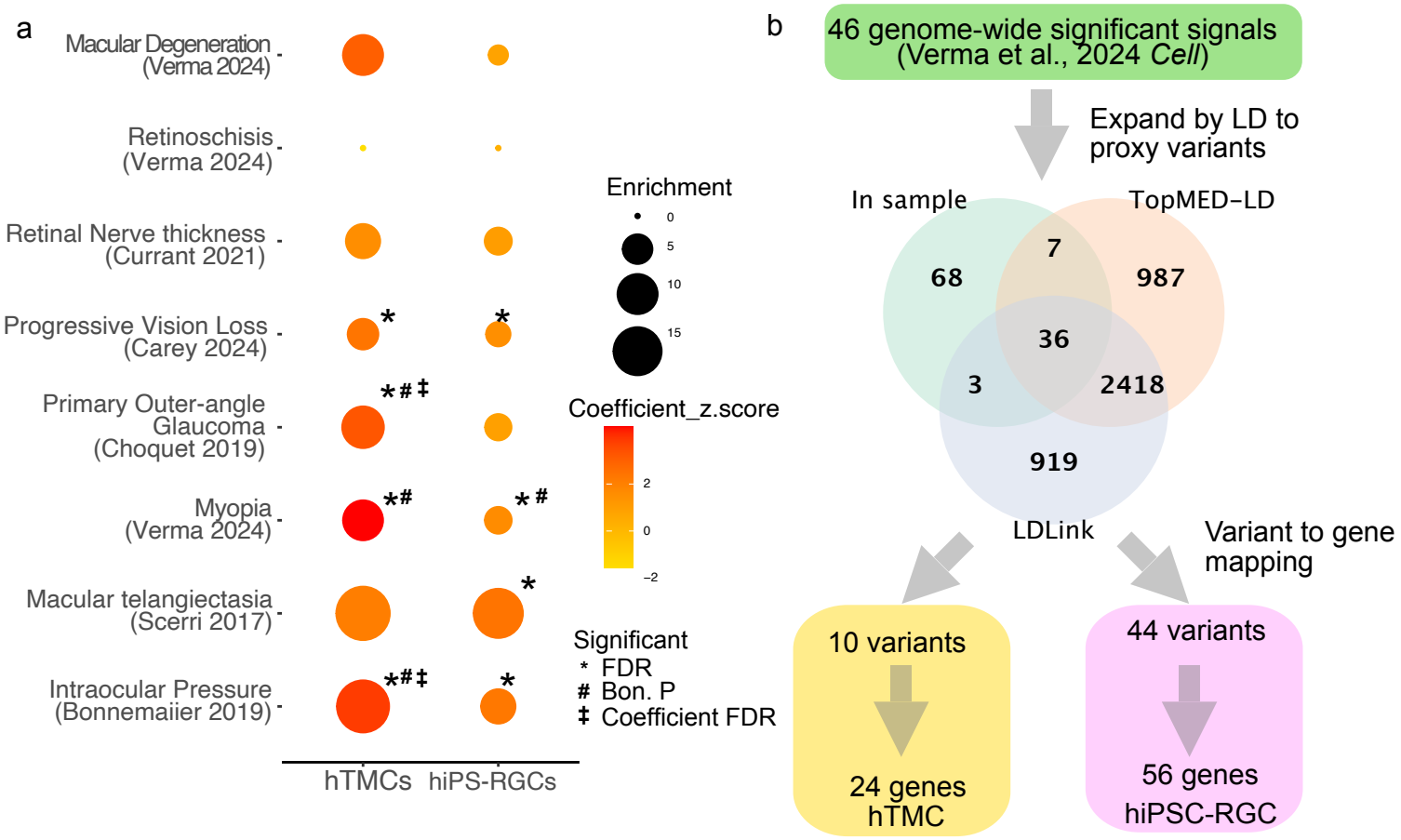

Figure 3: Dot plot depicting the results of partitioned LD score regression for hTMCs and hiPSC-RGCs across several European ancestry GWAS studies. Dot size depicts the size of enrichment and is colored by the coefficient z-score (higher corresponds to stronger association). *indicates the enrichment is significant following Bonferroni correction, # indicates the result is significant following FDR correction, and ‡ indicates significance of the baseline-adjusted cell type coefficient FDR. (b) To identify effector genes of risk loci identified in our African ancestry GWAS of POAG37, we expanded sentinel variants by LD (R2 > 0.6) using either the TOPMED-LD68 or LDLink69 reference databases. These variants were intersected with putative PIR-OCRs to identify the subset likely to be causal and their effector genes in hTMC and hiPSC-RGCs.

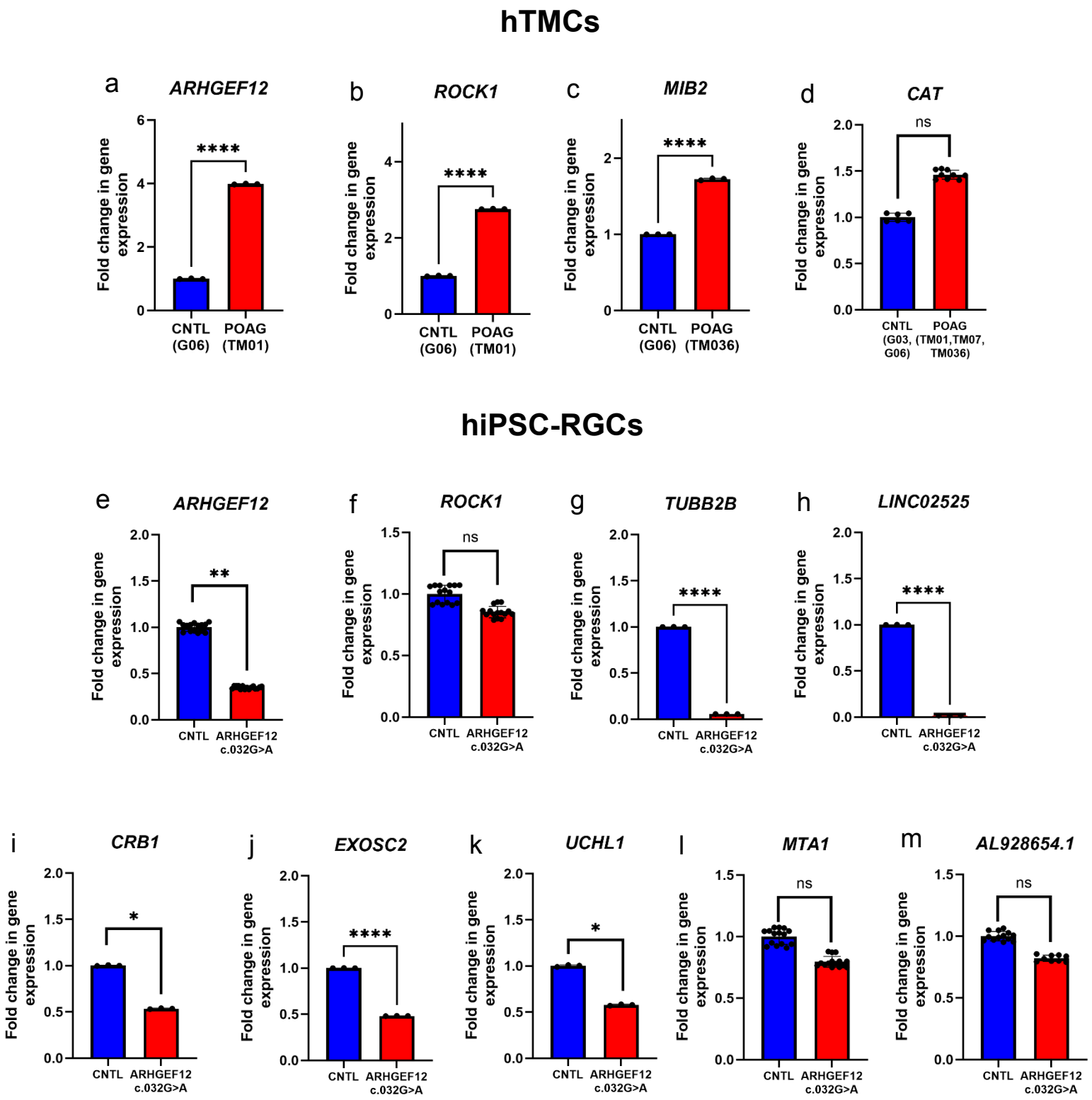

Figure 4: Quantitative mRNA expression analyses of prioritized genes implicated in hTMCs and hiPSC-RGCs. The quantitative expression profiles of the putative genes using qRT-PCR, in cell lines with and without POAG. In hTMCs, genes include: (a) *ARHGEF12*, (b) *ROCK1*, (c) *MIB2*, and (d) *CAT*. In hiPSC-RGCs, genes include: (e) *ARHGEF12*, (f) *ROCK1*, (g) *TUBB2B*, (h) *LINC02525*, (i) *CRB1*, (j) *EXOSC2*, (k) *UCHL1*, (l) *MTA1*, and (m) *AL928654.1*. CNTL= cells from a visually unaffected control subject and *ARHGEF12* c.032G>A= hiPSC-RGCs generated from a POAG subject with *ARHGEF12* SNP. Dots equal each technical replicate; *p<0.05, **p<0.01, ***p<0.001, ****p<0.0001.

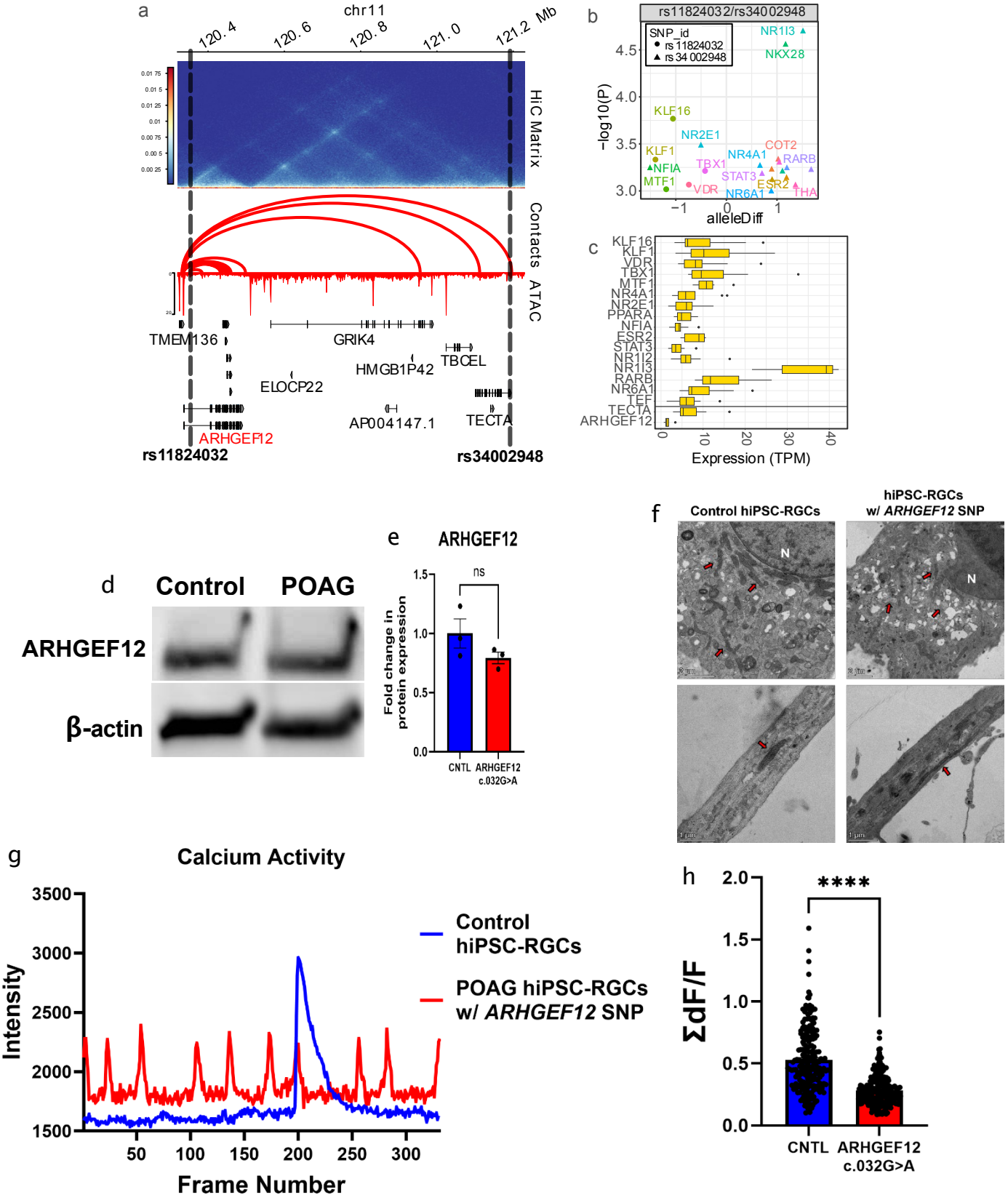

Figure 5: Nomination of *ARHGEF12* as a putative effector gene for African ancestry POAG in hiPSC-RGCs. (a) Genomic track showing contact frequency, promoter contacts, and chromatin accessibility for *ARHGEF12.* Two implicated SNPs, rs11824032 and rs34002948, are highlighted. (b) Motifs predicted to be disrupted by these variants (circles = rs11824032; triangles = rs34002948). The x-axis is the difference in information content (log scale) relative to the alternative/reference alleles, with the -log10 P value on the y-axis. Color corresponds to the transcription factor name. (c) The expression level of predicted transcription factors and implicated genes across each replicate of hiPSC-RGC in the *ARHGEF12* locus. (d) Western blots depicting ARHGEF12 protein and (e) quantification of the levels in control and POAG hiPSC-RGCs. (f) Transmission electron microscopy (TEM) images revealing ultrastructural analyses of morphological differences between control and *ARHGEF12* variant hiPSC-RGCs. Arrows pointing towards mitochondria and N: Nucleus. Scale bars as indicated. (g) Representative fluorescence responses from action potential firing in control and POAG hiPSC-RGCs. For simplicity, fluorescence from only one cell is shown for each condition. Note that the number of control RGCs exhibiting spontaneous Ca^2 responses is substantially greater than the number observed in POAG hiPSC-RGCs (see Videos 5a and 5b). (h) The total sum of all RGC amplitudes in control and *ARHGEF12* variant expressing hiPSC-RGCs. CNTL= hiPSC-RGCs from a visually unaffected control subject and *ARHGEF12* c.032G>A= hiPSC-RGCs generated from a POAG subject with *ARHGEF12* SNP. Dots equal the number of cells quantified in each technical replicate; *p<0.05, **p<0.01, ***p<0.001, ****p<0.0001.